95) Watanabe T, Bertoletti A, Tanoto TA. PD-1/PD-L1 pathway and T-cell exhaustion in chronic hepatitis virus infection. *J Viral Hepat*, 2010; 17: 453–458.
96) Kimura K, Kakimi K, Wieland S, Guidotti LG, Chisari FV. Activated intrahepatic antigen-presenting cells inhibit hepatitis B virus replication in the liver of transgenic mice. *J Immunol*, 2002; 169: 5188–5195.
97) Quezada SA, Jarvinen LZ, Lind EF, Noelle RJ. CD40/CD154 interactions at the interface of tolerance and immunity. *Annu Rev Immunol*, 2004; 22: 307–328.
98) Ito H, Ando K, Ishikawa T, Nakayama T, Taniguchi M, Saito K, Imawari M, Moriwaki H, Yokochi T, Kakumu S, Seishima M. Role of Vα14$^+$ NKT cells in the development of hepatitis B virus-specific CTL: activation of Vα14$^+$ NKT cells promotes the breakage of CTL tolerance. *Int Immunol*, 2008; 20: 869–879.
99) Livingston BD, Crimi C, Grey H, Ishioka G, Chisari FV, Fikes J, Grey H, Chesnut RW, Sette A. The hepatitis B virus-specific CTL responses induced in humans by lipopeptide vaccination are comparable to those elicited by acute viral infection. *J Immunol*, 1997; 159: 1383–1392.
100) Livingston BD, Alexander J, Crimi C, Oseroff C, Celis E, Daly K, Guidotti LG, Chisari FV, Fikes J, Chesnut RW, Sette A. Altered helper T lymphocyte function associated with chronic hepatitis B virus infection and its role in response to therapeutic vaccination in humans. *J Immunol*, 1999; 162: 3088–3095.
101) Ishikawa T, Kono D, Chung J, Fowler P, Theofilopoulos A, Kakumu S, Chisari FV. Polyclonality and multispecificity of the CTL response to a single viral epitope. *J Immunol*, 1998; 161: 5842–5850.
102) Xu DZ, Zhao K, Guo LM, Chen XY, Wang HF, Zhang JM, Xie Q, Ren H, Wang WX, Li LJ, Xu M, Liu P, Niu JQ, Bai XF, Shen XL, Yuan ZH, Wang XY, Wen YM. A randomized controlled phase IIb trial of antigen-antibody immunogenic complex therapeutic vaccine in chronic hepatitis B patients. *PLoS ONE*, 2008; 3: e2565.
103) Hamza T, Barnett JB, Li B. Interleukin 12 a key immunoregulatory cytokine in infection. *Int J Mol Sci*, 2010; 11: 789–806.
104) Rehermann B, Fowler P, Sidney J, Person J, Redeker A, Brown M, Moss B, Sette A, Chisari FV. The cytotoxic T lymphocyte response to multiple hepatitis B virus polymerase epitopes during and after acute viral hepatitis. *J Exp Med*, 1995; 181: 1047–1058.
105) Aguilar JC, Lobaina Y, Muzio V, García D, Pentón E, Iglesias E, Pichardo D, Urquiza D, Rodríguez D, Silva D, Petrovsky N, Guillén G. Development of a nasal vaccine for chronic hepatitis B infection that uses the ability of hepatitis B core antigen to stimulate a strong Th1 response against hepatitis B surface antigen. *Immunol Cell Biol*, 2004; 82: 539–546.
106) Betancourt AA, Delgado CA, Estéveza ZC, Martínez JC, Ríos GV, Aureoles-Rosellóc SRM, Zaldívara RA, Guzmána MA, N. Baile F, Reyes PAD, Ruano LO, Fernández AC, Lobaina-Matos Y, Fernández AD, Madrazo AIJ, Martínez MIA, Baños ML, Alvarez NP, Baldo MD, Mestre RES, Pérez MVP, Martínez MEP, Escobar DA, Guanche MJC, Cáceres LM, Betancourt RS, Rando EH, Nieto, GEG, González VLM, Rubido JCA. Phase I clinical trial in healthy adults of a nasal vaccine candidate containing recombinant hepatitis B surface and core antigens. *Int J Infect Dis*, 2007; 11: 394–401.
107) Mancini-Bourgine M, Fontaine H, Scott-Algara D, Pol S, Bréchot C, Michel ML. Induction or expansion of T-cell responses by a hepatitis B DNA vaccine administered to chronic HBV carriers. *Hepatology*, 2004; 40: 874–882.
108) Scott-Algara D, Mancini-Bourgine M, Fontaine H, Pol S, Michel ML. Changes to the natural killer cell repertoire after therapeutic hepatitis B DNA vaccination. *PLoS ONE*, 2010; 5: e8761.
109) Akbar SMF, Furukawa S, Horiike N, Abe M, Hiasa Y, Onji M. Safety and immunogenicity of hepatitis B surface antigen-pulsed dendritic cells in patients with chronic hepatitis B. *J Viral Hepat*, 2011; 18: 408–414.
110) Luo J, Li J, Chen RL, Nie L, Huang J, Liu ZW, Luo L, Yan XJ. Autologus dendritic cell vaccine for chronic hepatitis B carriers: a pilot, open label, clinical trial in human volunteers. *Vaccine*, 2010; 28: 2497–2504.

SCIENTIFIC REPORTS

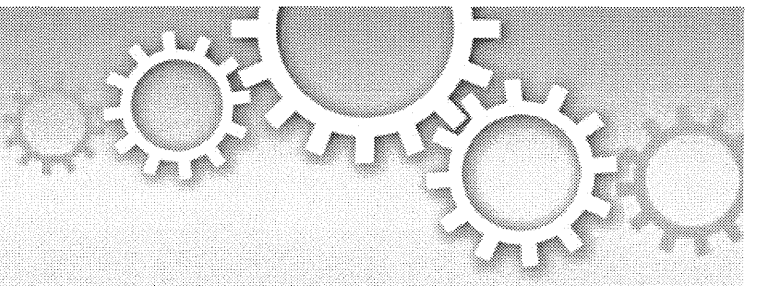

SUBJECT AREAS:
BIOLOGICAL MODELS
INNATE IMMUNITY
PATHOGENS
VIROLOGY

Received
16 March 2012

Accepted
29 March 2012

Published
16 April 2012

Correspondence and requests for materials should be addressed to H.I. (hito@gifu-u.ac.jp)

High susceptibility to lipopolysaccharide-induced lethal shock in encephalomyocarditis virus-infected mice

Hirofumi Ohtaki[1], Hiroyasu Ito[1], Masato Hoshi[1], Yosuke Osawa[1], Manabu Takamatsu[2], Akira Hara[2], Tetsuya Ishikawa[4], Hisataka Moriwaki[3], Kuniaki Saito[5] & Mitsuru Seishima[1]

[1]Department of Informative Clinical Medicine, [2]Department of Pathology, [3]First Department of Internal Medicine, Gifu University Graduate School of Medicine, 1-1 Yanagido, Gifu 501-1194, Japan, [4]Department of Medical Technology, Nagoya University School of Health Sciences, 1-20 Daikominami-1-chome, Higashi-ku, Nagoya, Aichi 461-8673, Japan, [5]Human Health Sciences, Graduate School of Medicine and Faculty of Medicine, Kyoto University, 53 Kawahara-cho, Shogoin, Sakyo, Kyoto 606-8507, Japan.

Secondary bacterial infection in humans is one of the pathological conditions requiring clinical attention. In this study, we examined the effect of lipopolysaccharide (LPS) on encephalomyocarditis virus (EMCV) infected mice. All mice inoculated with EMCV at 5 days before LPS challenge died within 24 h. LPS-induced TNF-α mRNA expression was significantly increased in the brain and heart at 5 days after EMCV infection. $CD11b^+/TLR4^+$ cell population in the heart was remarkably elevated at 5 days after EMCV infection, and sorted $CD11b^+$ cells at 5 days after EMCV infection produced a large amount of TNF-α on LPS stimulation *in vivo* and *in vitro*. In conclusion, we found that the infiltration of $CD11b^+$ cells into infected organs is involved in the subsequent LPS-induced lethal shock in viral encephalomyocarditis. This new experimental model can help define the mechanism by which secondary bacterial infection causes a lethal shock in viral encephalomyocarditis.

Polymicrobial infectious diseases show the involvement of 2 or more microbes, including viruses, bacteria, fungi or parasites, and these microbes act synergistically to mediate complex disease processes. In particular, a bacterial infection superimposed over an acute viral infection such as influenza is well known as the aggravation factor in the infectious disease[1,2]. Lipopolysaccharide (LPS), the outer membrane of gram-negative bacteria, causes systemic inflammatory response syndrome, endotoxic shock, disseminated intravascular coagulation and multi-organ failure[3,4]. LPS is recognized by Toll-like receptor 4 (TLR4)-expressing immunocompetent cells, mainly monocytes and macrophages, and induces the production of inflammatory cytokines through NF-κB activation[3]. Toxic effects of LPS are partially induced by the release and action of macrophage-derived inflammatory cytokines. Especially, the mass production of tumor necrosis factor-α (TNF-α) causes septic shock with an abrupt reduction in blood pressure, leading to rapid aggravation of the disease condition[5,6]. It is known that LPS-induced lethal shock is caused by a large quantity of TNF-α produced by immune cells activated by some kind of pre-stimulation[7,8].

Encephalomyocarditis virus (EMCV), which is a single-stranded RNA virus and a member of *Cardiovirus* in the Picornaviridae family, causes acute myocarditis and encephalitis in various animal species[9,10]. In some reports, including our previous study, the death of mice by EMCV infection of high density (500 plaque-forming units (pfu)) occurred after 6 days, and the mice that survived for 12 days subsequently recovered. Additionally, remarkable inflammation in the brain and heart occurred at around 6 days after EMCV infection, and thereafter the inflammation reduced as the days progressed. Hence, these results suggested that inflammatory cells reach the activating stage around 6 days after EMCV infection[11–13]. It was also demonstrated that various cells under the activating stage augment reactivity to LPS stimulation[14–16]. Previous studies showed that TNF-α is produced in large quantities by subsequent LPS stimulation during adenovirus infection[17], lymphocytic choriomeningitis virus, and varicella-zoster virus infection[18], but the original source of TNF-α is not elucidated. Moreover, it is unknown how LPS affects in the viral encephalomyocarditis. The aim of our study is to examine the effect of LPS

on EMCV-infected mice and to characterize the infiltrating cells, which possibly produce TNF-α, into the heart in this model.

Results

Survival of mice after LPS stimulation during EMCV infection. The mice were intraperitoneally inoculated with 20 pfu of EMCV and were intravenously injected with 10 μg LPS at 0, 2, and 5 days after the EMCV inoculation. At 5 days after EMCV infection, all mice died after LPS treatment within 24 h, but the mice subjected to this treatment at 0 and 2 days after EMCV infection were alive (Table 1). Moreover, at 5 days after EMCV infection, LPS-induced lethal shock developed in the mice in an LPS dose-dependent manner (Table 2).

To compare the survival rate between WT and TNF-α KO mice after LPS treatment during EMCV infection, the mice were treated intravenously with 10 μg LPS at 5 days after EMCV infection. All WT mice died after LPS treatment within 24 h at 5 days after EMCV infection, whereas TNF-α KO mice did not die. Moreover, LPS-induced lethality in WT mice was improved by anti-TNF-α antibody (100 μg/mouse) treatment before LPS stimulation (Table 3).

Effect of EMCV infection on LPS-induced TNF-α production. The concentration of serum TNF-α was measured at 0, 2, and 8 h after LPS treatment in each EMCV infection period. LPS-induced TNF-α concentration in the serum was markedly increased at 5 days after EMCV infection than at 0 and 2 days after EMCV infection (Fig. 1A).

For the localization of TNF-α production, TNF-α mRNA expression was determined in the brain, heart, liver, lung, and spleen at 0, 1, and 8 h after LPS treatment. TNF-α mRNA expression in the brain, heart, and liver of mice was significantly increased at 5 days after EMCV infection as compared with that at 0 and 2 days after EMCV infection (Fig. 1B).

Histopathological finding and viral load of the tissues after EMCV infection. Histological changes were observed in the brain and heart. The mice were inoculated intraperitoneally with 20 pfu of EMCV. Neuronal cell death and the presence of some inflammatory cells in hippocampus or brain surface of the brain and marked infiltration of inflammatory cells in the heart were seen at 5 days after EMCV infection. The infiltrating cells mainly included macrophages and neutrophils (Fig. 2A). In the liver, a little infiltration of inflammatory cells was observed at 5 days after EMCV infection, and no remarkable change was seen in the lung during each infection period (Data not shown). All tissues at 8 h after LPS treatment in EMCV-infected mice were not observed the significant increase of inflammatory cells in comparison with the tissues before LPS treatment (data not shown).

We measured the viral load in the brain, heart, liver, lung and spleen at 2 and 5 days after EMCV infection. Viral loads in all tissues at 5 days after EMCV infection were increased as compared with those at 2 days after EMCV infection. In particular, viral loads in the brain and heart markedly increased at 5 days after the infection (Fig. 2B).

Effect of EMCV infection on mRNA expression of chemokines in the tissues. Chemoattractant protein-1 (MCP-1) is a major chemoattractant responsible for the recruitment of macrophages[19,20].

Table 1 | Effect of LPS on lethality in EMCV-infected mice

Mouse	Days[a]	LPS (μg)	Lethality (dead/total)
Wild-type	0	10	0/10
Wild-type	2	10	0/10
Wild-type	5	10	10/10

[a]Days after EMCV infection.

Table 2 | Effect of various dose of LPS on lethality

Mouse	Days[a]	LPS (μg)	Lethality (dead/total)
Wild-type	5	0	0/8
Wild-type	5	1	1/8
Wild-type	5	5	6/8
Wild-type	5	10	8/8

[a]Days after EMCV infection.

macrophage inflammatory protein-2 (MIP-2) and keratinocyte-derived chemokine (KC), which are produced by macrophages, exhibit potent neutrophil chemotactic activity[21,22]. Because the infiltrated cells were mainly composed of macrophages and neutrophils as revealed by histopathological findings (Fig. 2A), the mRNA expressions of MCP-1, MIP-2, and KC were determined in the brain and heart at 0, 2, and 5 days after EMCV infection. The mRNA expression of these chemokines in the brain and heart on 5 days after EMCV infection was significantly up-regulated as compared with that at 0 and 2 days after EMCV infection (Fig. 3). MCP-1 mRNA expression at 5 days after EMCV infection was 808-fold in the brain and 125-fold in the heart based on 0 days. Similarly, MIP-2 mRNA expression was enhanced 254-fold in the brain and 44-fold in the heart, and KC mRNA expression was increased 23-fold in the brain and also in the heart. Although the expression of chemokines in the liver, lung and spleen had a tendency to up-regulated at 5 days after EMCV infection, the up-regulation was not more remarkable than that in the brain or heart.

Effect of EMCV infection on TLR4 mRNA expression in tissues and infiltrating cells in the heart. The expression of TLR4 mRNA was examined in the brain, heart, liver, lung and spleen at 0, 2, and 5 days after EMCV infection. TLR4 mRNA expression in the brain, heart, and liver at 5 days after EMCV infection was significantly increased. On the other hand, TLR4 mRNA expression in the lung and spleen showed no significant change after viral infection (Fig. 4A).

Next, we determined the phenotype of mononuclear cells (MNCs) from the heart at 5 days after EMCV infection. Although a lot of $CD11b^+TLR4^+$ cells were contained in MNCs from the heart at 5 days after EMCV infection, few $CD11c^+$, $CD3^+$, $CD19^+$ and $CD49b^+$ cells were contained (Fig. 4B).

LPS-induced TNF-α production in $CD11b^+$ cells from the heart *in vivo* and *in vitro*. Because MNCs from the heart at 5 days after EMCV infection were mainly occupied by $CD11b^+$ cells, we evaluated the ability of LPS-induced TNF-α production in $CD11b^+$ cells *in vivo*. The mice were intravenously inoculated with brefeldin A (250 μg/mouse) and LPS (10 μg/mouse) at 5 days after EMCV infection, and MNCs from the heart were harvested at 1 h after LPS treatment. TNF-α producing cell in gated $CD11b^+$ cells on the basis of isotype control were increased by LPS treatment (Fig. 5A).

Table 3 | Effect of LPS on lethality in TNF-α KO mice and wild-type mice treated with anti-TNF-α antibody

Mouse	Days[a]	LPS (μg)	Lethality (dead/total)
Wild-type	0	10	0/8
Wild-type	5	10	8/8
TNF-α KO	0	10	0/8
TNF-α KO	5	10	0/8
Wild-type + anti-TNF-α Ab	5	10	0/5

[a]Days after EMCV infection.

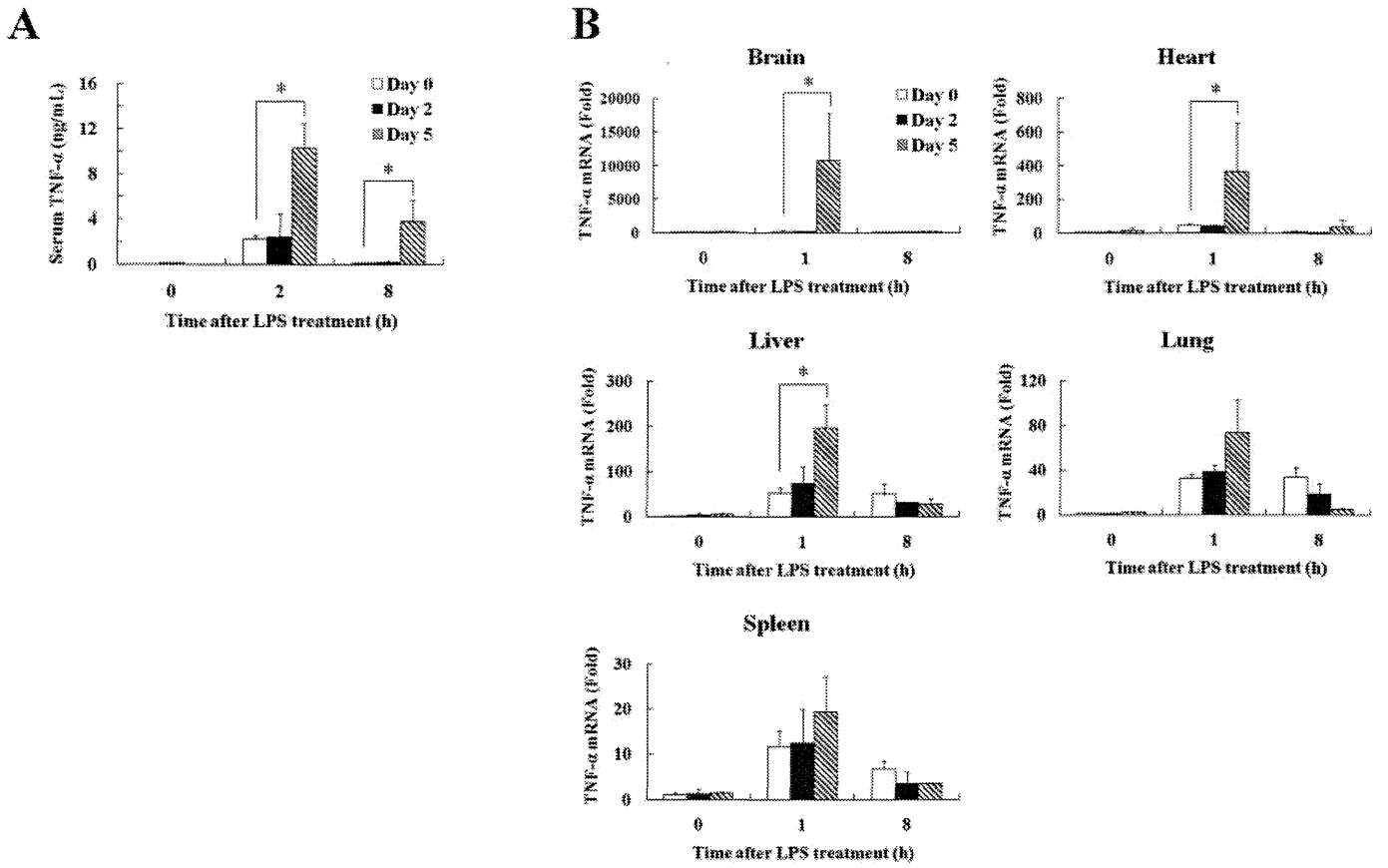

Figure 1 | Effect of EMCV infection on LPS-induced TNF-α production. The concentration of serum TNF-α was determined at 0, 2, and 8 h after LPS treatment in each EMCV infection period (A). TNF-α mRNA expression in the brain, heart, liver, lung, and spleen at 0, 1, and 8 h after LPS treatment in each EMCV infection period was determined on the basis of 18S rRNA expression using real-time RT-PCR. The data were calculated referring to mRNA levels of the respective tissues in control mice (0 days after EMCV infection, 0 hours after LPS inoculation) (B). The data are represented as means ± SD of the results of 4 mice in each group. *$p<0.05$

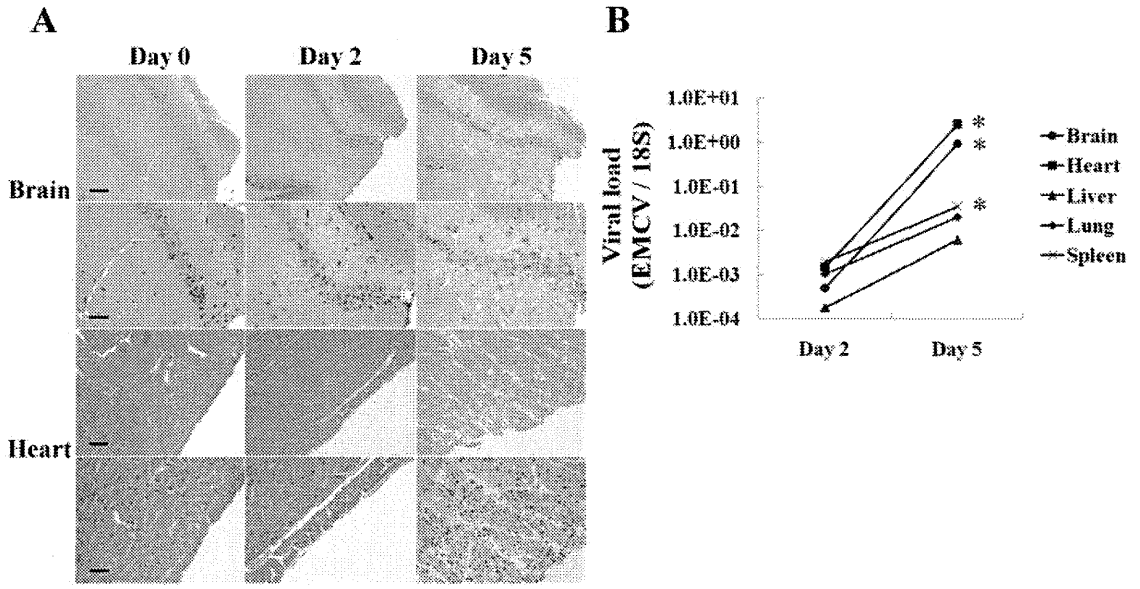

Figure 2 | Histopathological finding and viral load of the tissues after EMCV infection. Histopathological examination in the brain and heart at 0, 2 and 5 days after EMCV infection was performed. Tissue sections were deparaffinized, stained with hematoxylin-eosin, and examined under light microscopy. Scale bars, 200 μm (low-power field) and 50 μm (high-power field). These experiments were performed with 4 mice in each group and produced the same results (A). Viral RNA in the brain, heart, liver, lung, and spleen at 0, 2, and 5 days after EMCV infection was analyzed by real-time RT-PCR and was determined on the basis of 18S rRNA expression. The data are represented as means ± SD of the results of 4 mice in each group. The statistical analysis was performed by comparing with Day 2 (B). *$p<0.05$

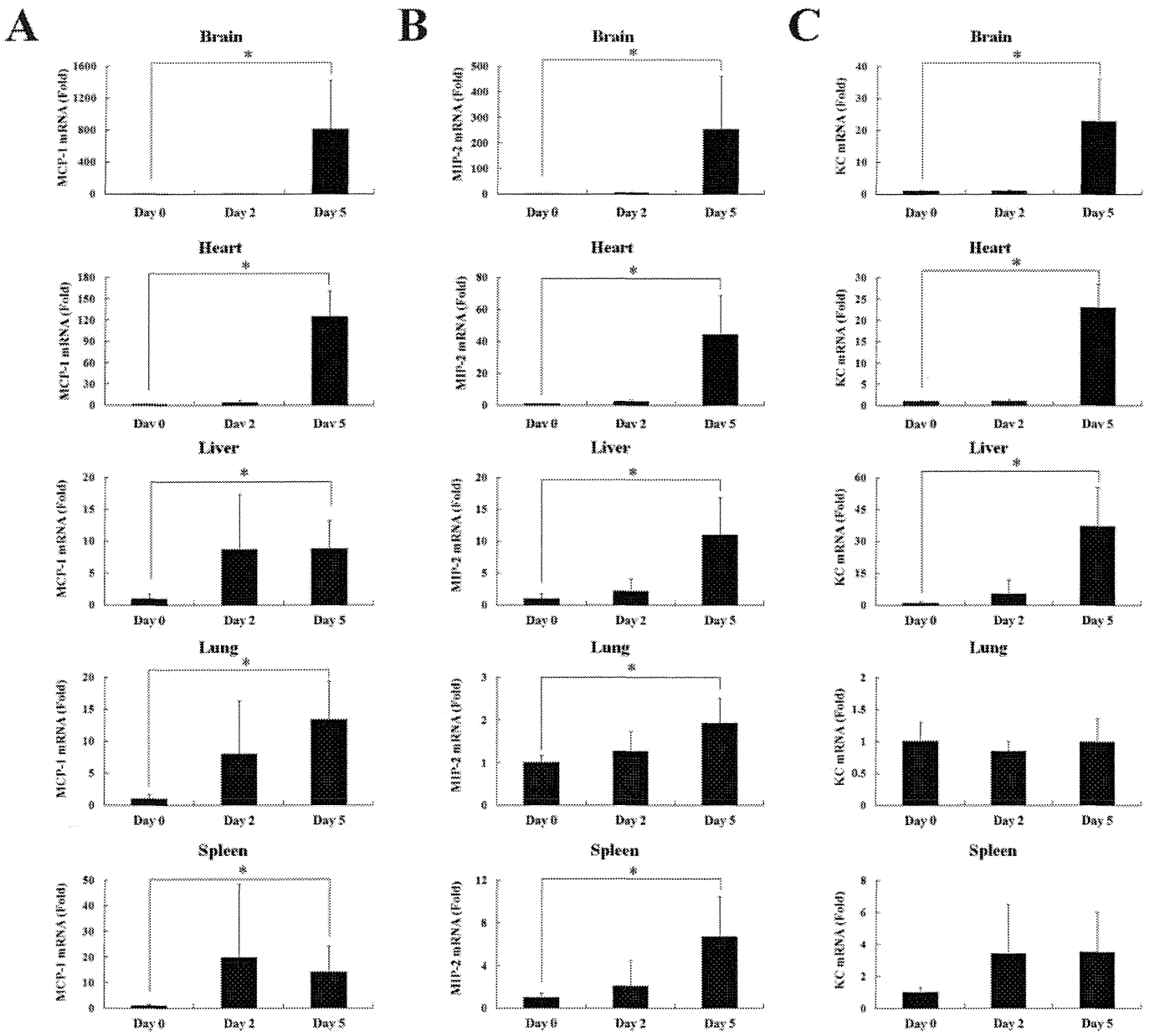

Figure 3 | Effect of EMCV infection on mRNA expression of chemokines in the tissues. The expression of MCP-1 (A), MIP-2 (B) and KC (C) mRNA in the brain, heart, liver, lung and spleen at 0, 2 and 5 days after EMCV infection was analyzed by real-time RT-PCR and was determined on the basis of 18S rRNA expression. The data were calculated referring to mRNA levels of the respective tissues in control mice (Day 0). The data are represented as means ± SD of the results of 6 mice in each group. $*p<0.05$

$CD11b^+$ and $CD11b^-$ cells from the heart at 5 days after EMCV infection were isolated by magnetic cell sorting. Isolated cells and total cells before isolation were cultured at 1×10^5 cells/200 μL with LPS (1 μg/mL) for 24 h. LPS-induced TNF-α production in $CD11b^+$ cells was significantly increased as compared with that in total cells and $CD11b^-$ cells. $CD11b^-$ cells could not produce TNF-α after LPS stimulation (Fig. 5B).

Discussion

In this study, we demonstrated that LPS treatment at 5 days after EMCV infection induces an excess of TNF-α production in the brain and heart and lethal shock (Table 1, Fig. 1). Because this lethal effect of LPS was cancelled out in TNF-α KO mice infected with EMCV (Table 3), it is likely that TNF-α from the brain and heart plays a critical role in the lethal effect of LPS on EMCV infection. Septic shock is characterized by hypotension, decreased systemic vascular resistance and impaired vascular reactivity, and TNF-α has been implicated as a principal mediator in the pathogenesis of septic shock[23]. TNF-α is mainly produced by macrophages in the peripheral tissue after pathogen infection, and is involved in the elimination of pathogens from the host[24,25]. A protective role of TNF-α in EMCV-infected mouse model is previously reported[11]. In contrast, an excessive production of TNF-α induces hypothermia, hypotension, multiple organ failure, septic shock, and death[5,6]. In particular, previous reports demonstrated that the macrophages treated with some pre-stimulants produce a large amount of TNF-α on subsequent LPS stimulation. *Propionibacterium acnes,* an anaerobic gram-positive bacterium, exerts strong immunomodulatory activities, and participates in the formation of intrahepatic granulomas and induction of hypersensitivity for LPS in mice. Additionally, these activities depended on the recognition of bacteria via TLR9 and subsequent IL-12-mediated IFN-γ production[26,27]. EMCV infection also

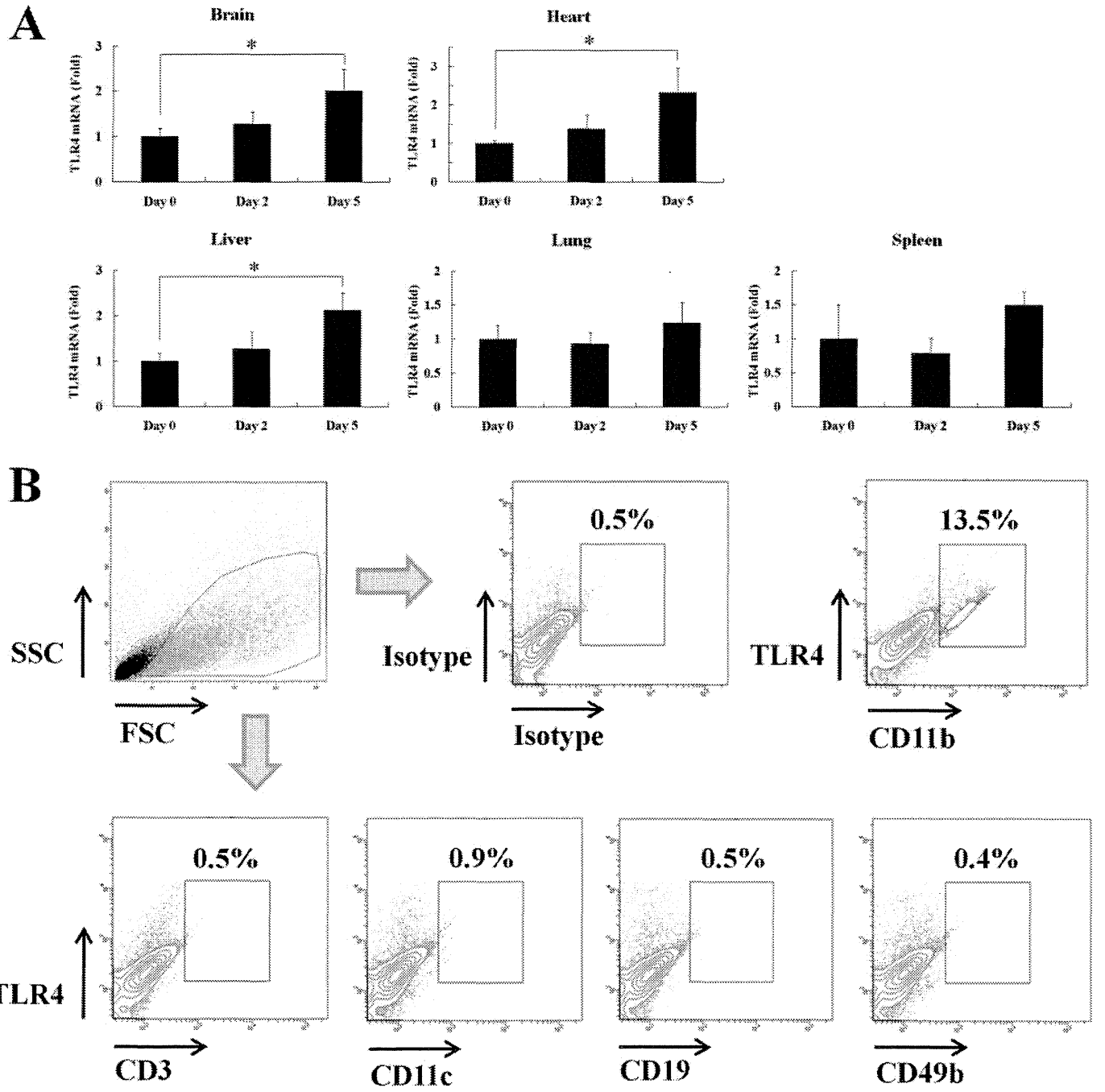

Figure 4 | Effect of EMCV infection on TLR4 mRNA expression in tissues and infiltrating cells in the heart. The expression TLR4 mRNA in the brain, heart, liver, lung, and spleen at 0, 2, and 5 days after EMCV infection was analyzed by real-time RT-PCR and was determined on the basis of 18S rRNA expression. The data were calculated referring to mRNA levels of the respective tissues in control mice (Day 0). The data are represented means ± SD from 4 mice of each group (A). Following reaction with anti-CD16/CD32 antibody to suppress nonspecific binding, MNCs from the heart were stained with anti-CD3ε, anti-CD11b, anti-CD11c, anti-CD19, anti-CD49b and anti-TLR4 antibody. The positive rate of the cells was made on the basis of isotype control. The data are representative of three separate experiments (B). *$p<0.05$

markedly increased the LPS-induced TNF-α mRNA level and viral road in the brain and heart (Fig. 1B, 2B). Namely, the susceptibility to LPS was enhanced in the EMCV-infected site.

TLR4 recognizes LPS from gram-negative bacteria, and its recognition is essential for the activation of the innate immune system. In humans with myocarditis, TLR4 mRNA is also increased in the heart[28]. In the present study, the mRNA expression of TLR4 in the brain, heart, and liver was increased after EMCV infection (Fig. 4A), and a significant increase in TNF-α mRNA expression was also confirmed after subsequent LPS stimulation (Fig. 1B). Histological findings revealed neuronal cell death and the presence of some inflammatory cells in hippocampus or brain surface of the brain, remarkable infiltration of inflammatory cells in the heart, and a little infiltration of inflammatory cells in the liver at 5 days after EMCV infection; further, the infiltrating cells were mainly composed of macrophages and neutrophils. These results indicate that the accumulation of inflammatory cells in the heart after EMCV infection is associated with this lethal septic shock model. In fact, there is a correlation between TLR4 mRNA expression and the number of infiltrated TLR4 positive cells in the heart. A previous report also

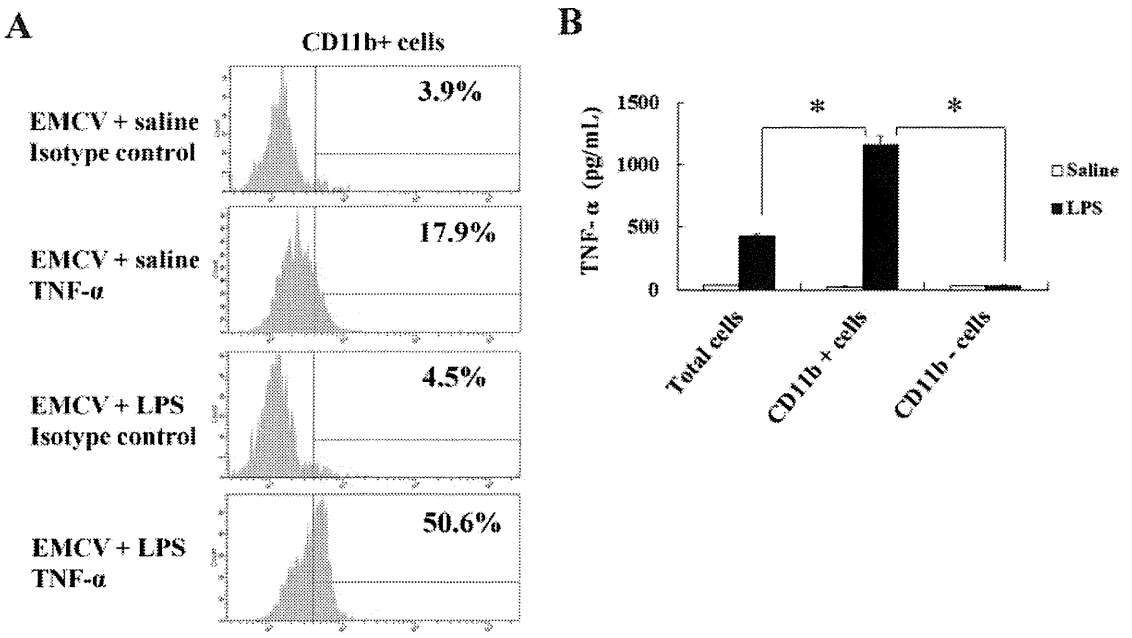

Figure 5 | LPS-induced TNF-α production in CD11b$^+$ cells from the heart *in vivo* and *in vitro*. The mice were inoculated intravenously with brefeldin A (250 μg/mouse) and LPS (10 μg/mouse) at 5 days after EMCV infection, and MNCs from the heart were harvested at 1 h after LPS treatment. MNCs were stained with anti-CD11b and anti-TNF-α antibody. The data are representative of three separate experiments (A). Isolated CD11b$^+$ and CD11b$^-$ MNCs and total cells before isolation were cultured at 1×10^5 cells per 200 μL with LPS (1 μg/mL) for 24 h. The concentration of TNF-α was determined in culture supernatant. The data are represented means ± SD in triplicate cultures (B). *$p<0.05$

demonstrated the augmentation of TLR4 mRNA expression by infiltration of TLR4-positive leukocytes into the liver in an IL-17-induced multiple tissue inflammation model[29]. Furthermore, our previous studies proved the infiltration of TLR4-positive leukocytes into the liver on α-galactosylceramide administration and the excessive response to subsequent LPS stimulation[8,15]. In this study, CD11b$^+$/TLR4$^+$ cells in the heart increased at 5 days after EMCV infection, but few CD11c$^+$, CD3$^+$, CD19$^+$ and CD49b$^+$ cells were contained (Fig. 4B). LPS-induced TNF-α was mainly produced by CD11b$^+$ cells in the heart at 5 days after EMCV infection *in vivo* and *in vitro* (Fig. 5). Therefore, it is suggested that the infiltration of CD11b$^+$ cells into the heart involves in the up-reguration of TLR4 mRNA and subsequent LPS induced TNF-α production.

mRNA expression of MCP-1, MIP-2, and KC in the brain and heart at 5 days after EMCV infection was markedly increased than that in uninfected mice (Fig. 3). The enhancement of the mRNA expression of these chemokines, especially MCP-1, may be involved in the infiltration of inflammatory cells into the heart. MCP-1 acts as a potent chemoattractant and activator of monocytes/macrophages[19,20]. Shiratsuchi et al[30] showed that macrophages phagocytose influenza virus-infected HeLa cells in a manner mediated by phosphatidylserine that appears on the surfaces of infected cells during the process of apoptosis. In addition, the inhibition of macrophage recruitment by MCP-1 augmented alveolar epithelial damage and apoptosis during influenza pneumonitis[31]. Thus, MCP-1 has an effective role in viral clearance, but it also may aggravate lethal shock by subsequent LPS stimulation under the EMCV-infected state.

Although the mice treated with 500 μg LPS died within 48 to 72 h in the general LPS-induced shock model[32,33], all mice treated with 10 μg LPS died within 24 hours in our model; this suggests that LPS susceptibility in mice markedly rises under the EMCV-infected condition. It is known that infection by the influenza virus, coxsackie virus, and adenovirus are involved in the onset of viral encephalitis or myocarditis[34,35], but there are few reports showing the effect of the secondary bacterial superimposed infection on viral encephalomyocarditis and its mechanism. In the present study, even a low-dose of LPS could cause the lethal septic shock in EMCV-infected mice. Thus, it is necessary to monitor serum endotoxin levels and prevent bacterial infection in patients with encephalitis and myocarditis.

In conclusion, we established a septic shock model using mice with viral encephalomyocarditis and demonstrated that the infiltration of CD11b$^+$ cells into tissues is involved in this lethal shock. From an immunological point of view, our animal model is useful for investigating the pathological state of bacterial superimposed infection on viral encephalomyocarditis.

Methods

Reagents. LPS from *Escherichia coli* O111:B5 and brefeldin A were purchased from Sigma-Aldrich (St Louis, MO, USA). Mouse TNF-α antibody (monoclonal rat IgG1) for neutralize was purchased from R&D Systems (Minneapolis, MN, USA).

Mice. Mouse experiments were performed according to the guidelines of the Animal Ethics Committee of Gifu University Graduate School of Medicine. C57BL/6J mice aged approximately 8–10 weeks were obtained from Japan SLC (Hamamatsu, Japan) and used as wild-type (WT) mice. TNF-α gene knockout (TNF-α KO) mice of a C57BL/6J background were produced by gene targeting as described previously[11,36,37].

Viral inoculation and LPS treatment. A myocarditic variant of EMCV was generously provided by Dr. Seto (Keio University, Tokyo, Japan). The virus stock was stored at −80°C in Hanks' balanced salt solution (HBSS) with 0.1% BSA required for use. The mice were inoculated intraperitoneally with 20 pfu of EMCV in 0.2 mL saline and were treated intravenously with 10 μg LPS in 0.2 mL saline at 0 (non-infected), 2, and 5 days after the viral inoculation unless otherwise noted. The lethality was determined at 24 h after LPS treatment. The experiments were performed according to the institutional guidelines of Gifu University for microbiologic study.

Measurement of serum TNF-α concentration. The concentration of TNF-α in the serum and culture supernatant was determined using a mouse TNF-α Quantikine ELISA kit (R&D Systems, Minneapolis, MN, USA), according to the manufacturer's recommendations.

Real-time RT-PCR analysis. Real-time RT-PCR was used to quantify the levels of TNF-α, TLR4, MCP-1, MIP-2, KC mRNA, and EMCV RNA. Total RNA in the brain, heart, liver, lung and spleen was isolated using Isogen (Nippon Gene, Tokyo, Japan) and transcribed to cDNA by using the High capacity cDNA transcription kit (Applied Biosystems, Foster City, CA, USA). Purified cDNA was used as the template for real-time PCR conducted using pre-designed primer/probe sets for TNF-α, TLR4, MCP-1, MIP-2, KC and 18S rRNA (Applied Biosystems), according to the manufacturer's recommendations. The determination of EMCV RNA was performed by the use of the LightCycler DNA Master SYBR Green I (Roche Diagnostic Systems, Indianapolis,

IN, USA) and the following oligonucleotide primer pairs: EMCV sense, 5′-GTCGTGAAGGAAGCAGTTCC-3′, antisense, 5′-CACGTGGCTTTTGGCCGCAGAGGC-3′[11]. 18S rRNA was used as an internal control. Real-time PCR was carried out using a Light-Cycler rapid thermal cycler system (Roche Diagnostic Systems).

Histological examination. Histopathological examination of the brain and heart was performed at 0, 2, and 5 days after EMCV infection. The tissues were fixed in 10% formalin in PBS for 48 h and embedded in paraffin. Tissue sections were deparaffinized, stained with H&E, and examined under light microscopy.

Cell isolation in heart. Single cells from the heart, particularly non-parenchymal cells, were isolated in reference to a previous report[38]. The heart was minced with scissors and was shaken with 5 mL HBSS containing collagenase type 2 (600 U/mL) and deoxyribonuclease I (60 U/mL) (Worthington, Lakewood, NJ, USA) for 30 min at 37°C. The specimen was filtered through a stainless steel mesh, and red blood cells were lysed. After washing and filtration through a 70-μm cell strainer, the single cells were suspended in RPMI 1640 medium (Wako Pure Chemical Industries; Osaka, Japan) containing 10% heat-inactivated fetal bovine serum (Thermo Fisher Scientific Inc, Waltham, MA, USA) and cultured at 37°C in a 5% CO_2 atmosphere.

Flow cytometry analysis. MNCs from the heart at 5 days after EMCV infection were obtained by centrifugation of the single cells with Ficoll-Conray (IBL, Gunma, Japan). Flow cytometry was used to evaluate the expression level of CD3, CD11b, CD11c, CD19, CD49b and TLR4 in MNCs from the heart at 5 days after EMCV infection. Following reaction with anti-CD16/CD32 antibody to suppress nonspecific binding, MNCs were stained with FITC-conjugated hamster anti-mouse CD3ε antibody (clone 145-2C11; BD Biosciences, Franklin Lakes, NJ, USA), FITC-conjugated rat anti-mouse CD11b antibody (clone M1/70; eBioscience, San Diego, CA, USA), FITC-conjugated hamster anti-mouse CD11c antibody (clone HL-3; BD Biosciences), FITC-conjugated mouse anti-mouse CD19 antibody (clone MB19-1; eBioscience), FITC-conjugated rat anti-mouse CD49b antibody (clone DX5; eBioscience), and PE-conjugated rat anti-mouse TLR4/MD2 complex antibody (clone MTS510; eBioscience). The positive rate of the cells was made on the basis of isotype control. The phenotypic characterization of the cells was carried out using FACSCanto II (BD Biosciences).

Intracellular cytokine staining *in vivo*. The mice were intravenously inoculated with brefeldin A (250 μg/mouse) and LPS (10 μg/mouse) at 5 days after EMCV infection. MNCs from the heart at 1 h after LPS treatment were fixed and permeabilized with the Cytofix/Cytoperm buffer (BD Biosciences) and were stained with PE-conjugated rat anti-TNF-α antibody (clone MP6-XT22; eBioscience). The cells were analyzed using FACSCanto II (BD Biosciences).

Isolation of CD11b$^+$ cells. MNCs from the heart obtained at 5 days after EMCV infection were separated into CD11b$^+$ and CD11b$^-$ cells using anti-CD11b-conjugated magnetic beads (Miltenyi Biotec GmbH, Bergisch Gladbach, Germany). The magnetically labeled cells were purified using the QuadroMACS separation unit attached to a MACS multistand and LS columns (Miltenyi Biotec GmbH).

Statistical analysis. In each experiment, the results were expressed as the mean ± SD. The statistical significance of the difference in mean values was determined by Student's *t* test or one-way analysis of variance followed by Scheffe's test. *P* values of less than 0.05 were considered significant.

1. Bakaletz, L. O. Developing animal models for polymicrobial diseases. *Nat. Rev. Microbiol.* **2**, 552–568 (2004).
2. Brundage, J. F. Interactions between influenza and bacterial respiratory pathogens: implications for pandemic preparedness. *Lancet Infect. Dis.* **6**, 303–312 (2006).
3. Cohen, J. The immunopathogenesis of sepsis. *Nature* **420**, 885–891 (2002).
4. Bannerman, D. D. & Goldblum, S. E. Direct effects of endotoxin on the endothelium: barrier function and injury. *Lab Invest* **79**, 1181–1199 (1999).
5. Tracey, K. J. & Cerami, A. Tumor necrosis factor: a pleiotropic cytokine and therapeutic target. *Annu Rev Med* **45**, 491–503 (1994).
6. Brouckaert, P. & Fiers, W. Tumor necrosis factor and the systemic inflammatory response syndrome. *Curr Top Microbiol Immunol* **216**, 167–187 (1996).
7. Gumenscheimer, M., Mitov, I., Galanos, C. & Freudenberg, M. A. Beneficial or deleterious effects of a preexisting hypersensitivity to bacterial components on the course and outcome of infection. *Infect Immun* **70**, 5596–5603 (2002).
8. Ito, H. *et al.* Lethal endotoxic shock using alpha-galactosylceramide sensitization as a new experimental model of septic shock. *Lab Invest* **86**, 254–261 (2006).
9. Kishimoto, C., Kuribayashi, K., Masuda, T., Tomioka, N. & Kawai, C. Immunologic behavior of lymphocytes in experimental viral myocarditis: significance of T lymphocytes in the severity of myocarditis and silent myocarditis in BALB/c-nu/nu mice. *Circulation* **71**, 1247–1254 (1985).
10. Topham, D. J., Adesina, A., Shenoy, M., Craighead, J. E. & Sriram, S. Indirect role of T cells in development of polioencephalitis and encephalomyelitis induced by encephalomyocarditis virus. *J Virol* **65**, 3238–3245 (1991).
11. Wada, H. *et al.* Tumor necrosis factor-alpha (TNF-alpha) plays a protective role in acute viralmyocarditis in mice: A study using mice lacking TNF-alpha. *Circulation* **103**, 743–749 (2001).
12. Yamamoto, K. *et al.* Attenuation of virus-induced myocardial injury by inhibition of the angiotensin II type 1 receptor signal and decreased nuclear factor-kappa B activation in knockout mice. *J Am Coll Cardiol* **42**, 2000–2006 (2003).
13. Nasu-Nishimura, Y. *et al.* Cellular prion protein prevents brain damage after encephalomyocarditis virus infection in mice. *Arch Virol* **153**, 1007–1012 (2008).
14. Ito, H. *et al.* Augmentation of lipopolysaccharide-induced nitric oxide production by alpha-galactosylceramide in mouse peritoneal cells. *J Endotoxin Res* **11**,213–219 (2005).
15. Ohtaki, H. *et al.* Valpha14 NKT cells activated by alpha-galactosylceramide augment lipopolysaccharide-induced nitric oxide production in mouse intrahepatic lymphocytes. *Biochem Biophys Res Commun* **378**, 579–583 (2009).
16. Ohtaki, H. *et al.* Interaction between LPS-induced NO production and IDO activity in mouse peritoneal cells in the presence of activated Valpha14 NKT cells. *Biochem Biophys Res Commun* **389**, 229–234 (2009).
17. Fejer, G. *et al.* Adenovirus infection dramatically augments lipopolysaccharide-induced TNF production and sensitizes to lethal shock. *J Immunol* **175**, 1498–1506 (2005).
18. Nansen, A. & Randrup Thomsen, A. Viral infection causes rapid sensitization to lipopolysaccharide: central role of IFN-alpha beta. *J Immunol* **166**, 982–988 (2001).
19. Matsushima, K., Larsen, C. G., DuBois, G. C. & Oppenheim, J. J. Purification and characterization of a novel monocyte chemotactic and activating factor produced by a human myelomonocytic cell line. *J Exp Med* **169**, 1485–1490 (1989).
20. Jiang, Y., Beller, D. I., Frendl, G. & Graves, D. T. Monocyte chemoattractant protein-1 regulates adhesion molecule expression and cytokine production in human monocytes. *J Immunol* **148**, 2423–2428 (1992).
21. Driscoll, K. E. Macrophage inflammatory proteins: biology and role in pulmonary inflammation. *Exp Lung Res* **20**, 473–490 (1994).
22. Lira, SA. *et al.* Expression of the chemokine N51/KC in the thymus and epidermis of transgenic mice results in marked infiltration of a single class of inflammatory cells. *J Exp Med* **180**, 2039–2048 (1994).
23. Tracey, K. J. *et al.* Anti-cachectin/TNF monoclonal antibodies prevent septic shock during lethal bacteraemia. *Nature* **330**, 662–664 (1987).
24. Sergerie, Y., Rivest, S. & Boivin, G. Tumor necrosis factor-alpha and interleukin-1 beta play a critical role in the resistance against lethal herpes simplex virus encephalitis. *J Infect Dis* **196**, 853–860 (2007).
25. Bekker, L. G. *et al.* Immunopathologic effects of tumor necrosis factor alpha in murine mycobacterial infection are dose dependent. *Infect Immun* **68**, 6954–6961 (2000).
26. Tchaptchet, S. *et al.* Innate, antigen-independent role for T cells in the activation of the immune system by Propionibacterium acnes. *Eur J Immunol* **40**, 2506–2516 (2010).
27. Inatsu, A. *et al.* Novel mechanism of C-reactive protein for enhancing mouse liver innate immunity. *Hepatology* **49**, 2044–2054 (2009).
28. Satoh, M. *et al.* Expression of Toll-like receptor 4 is associated with enteroviral replication in human myocarditis. *Clin Sci (Lond)* **104**, 577–584 (2003).
29. Tang, H. *et al.* TLR4 activation is required for IL-17-induced multiple tissue inflammation and wasting in mice. *J Immunol* **185**, 2563–2569 (2010).
30. Shiratsuchi, A., Kaido, M., Takizawa, T. & Nakanishi, Y. Phosphatidylserine-mediated phagocytosis of influenza A virus-infected cells by mouse peritoneal macrophages. *J Virol* **74**, 9240–9244 (2000).
31. Narasaraju, T., Ng, H. H., Phoon, M. C. & Chow, V. T. MCP-1 antibody treatment enhances damage and impedes repair of the alveolar epithelium in influenza pneumonitis. *Am J Respir Cell Mol Biol* **42**, 732–743 (2010).
32. Jung, ID. *et al.* Blockade of indoleamine 2,3-dioxygenase protects mice against lipopolysaccharide-induced endotoxin shock. *J Immunol* **182**, 3146–3154 (2009).
33. Liu, J. *et al.* The circadian clock Period 2 gene regulates gamma interferon production of NK cells in host response to lipopolysaccharide-induced endotoxic shock. *Infect Immun* **74**, 4750–4756 (2006).
34. Morishima, T. *et al.* Encephalitis and encephalopathy associated with an influenza epidemic in Japan. *Clin Infect Dis* **35**, 512–517 (2002).
35. Yajima, T. & Knowlton, KU. Viral myocarditis: from the perspective of the virus. *Circulation* **119**, 2615–2624 (2009).
36. Taniguchi, T., Takata, M., Ikeda, A., Momotani, E. & Sekikawa, K. Failure of germinal center formation and impairment of response to endotoxin in tumor necrosis factor alpha-deficient mice. *Lab Invest* **77**, 647–658 (1997).
37. Ito, H. *et al.* Role of TNF-alpha produced by nonantigen-specific cells in a fulminant hepatitis mouse model. *J Immunol* **182**, 391–397 (2009).
38. Pfister, O. *et al.* CD31- but Not CD31+ cardiac side population cells exhibit functional cardiomyogenic differentiation. *Circ Res* **97**, 52–61 (2005).

Author contributions

HO, HI and MS designed the project. HO, HI, YO, AH, TI, HM, KS and MS designed experiments. HO, MH and MT performed the experimental work. HO, HI and MS prepared the manuscript and figures. All authors reviewed the manuscript.

Additional information

Competing financial interests: The authors declare no competing financial interests.

How to cite this article: Ohtaki, H. *et al.* High susceptibility to lipopolysaccharide-induced lethal shock in encephalomyocarditis virus-infected mice. *Sci. Rep.* **2**, 367; DOI:10.1038/srep00367 (2012).

Systemic Circulation and Bone Recruitment of Osteoclast Precursors Tracked by Using Fluorescent Imaging Techniques

Manato Kotani,*,† Junichi Kikuta,*,† Frederick Klauschen,‡ Takenao Chino,§ Yasuhiro Kobayashi,¶ Hisataka Yasuda,‖ Katsuto Tamai,§ Atsushi Miyawaki,# Osami Kanagawa,** Michio Tomura,**,†† and Masaru Ishii*,†

Osteoclasts are bone-resorbing polykaryons differentiated from monocyte/macrophage-lineage hematopoietic precursors. It remains unclear whether osteoclasts originate from circulating blood monocytes or from bone tissue–resident precursors. To address this question, we combined two different experimental procedures: 1) shared blood circulation "parabiosis" with fluorescently labeled osteoclast precursors, and 2) photoconversion-based cell tracking with a Kikume Green-Red protein (KikGR). In parabiosis, CX_3CR1-EGFP knock-in mice in which osteoclast precursors were labeled with EGFP were surgically connected with wild-type mice to establish a shared circulation. Mature $EGFP^+$ osteoclasts were found in the bones of the wild-type mice, indicating the mobilization of $EGFP^+$ osteoclast precursors into bones from systemic circulation. Receptor activator for NF-κB ligand stimulation increased the number of $EGFP^+$ osteoclasts in wild-type mice, suggesting that this mobilization depends on the bone resorption state. Additionally, $KikGR^+$ monocytes (including osteoclast precursors) in the spleen were exposed to violet light, and 2 d later we detected photoconverted "red" $KikGR^+$ osteoclasts along the bone surfaces. These results indicate that circulating monocytes from the spleen entered the bone spaces and differentiated into mature osteoclasts during a certain period. The current study used fluorescence-based methods clearly to demonstrate that osteoclasts can be generated from circulating monocytes once they home to bone tissues. *The Journal of Immunology*, **2013, 190: 605–612.**

Osteoclasts are the only somatic cells that can destroy or resorb calcified bone tissues. Although it has been established that they originate from monocyte/macrophage-lineage hematopoietic precursors (1, 2), there is still controversy concerning their proximal precursors. Several studies have identified "osteoclast precursors" by detecting surface markers such as CD11b/Mac-1, Gr-1, receptor activator for NF-κB (RANK), and c-Fms (3–5), and lipid mediators and some chemokines, including sphingosine-1-phosphate (S1P) and SDF-1/CXCL12, have been shown to be involved in controlling their migration and localization in bone tissues (6, 7). However, monocyte-lineage cells are plastic, and no exclusive definition of osteoclast precursors similar to that proposed for lymphoid cell lineage commitment has been established (8, 9). More importantly, it is still unclear whether osteoclasts are derived from circulating monocytes or from bone tissue–resident precursors that are fully committed to differentiate into osteoclasts. In general, most tissue-resident macrophages, including Langerhans cells in the skin and microglia in the brain, have the potential to self-renew locally under steady-state conditions (10–12), although these cells can also be repopulated from circulating monocytoid precursors under certain pathological conditions and after artificial ablation (10, 12). What about osteoclasts? Bone tissue is highly vascularized and large numbers of fenestrations in the vessel walls increase blood permeability in this region (13). These unique features of bone are assumed to affect the mode of recruitment of osteoclast precursors.

By visualizing live bone tissues by intravital multiphoton microscopy, we recently demonstrated the migration of osteoclast precursors to and from the bone marrow vasculature, a process that was critically regulated by S1P, a lipid mediator that is present at high levels in plasma (14, 15). Other reports have suggested that osteoclast precursors that are fully committed to differentiation into osteoclasts are cell cycle quiescent and seem to circulate from hematopoietic tissues via the bloodstream onto the bone surfaces, where they differentiate (4, 5). However, there is no direct evidence for the systemic circulation of osteoclast precursor monocytes.

*Laboratory of Cellular Dynamics, World Premier International Research Center Initiative-Immunology Frontier Research Center, Osaka University, Suita, Osaka 565-0871, Japan; †Japan Science and Technology Agency, Core Research for Evolutionary Science and Technology, Chiyoda-ku, Tokyo 102-0075, Japan; ‡Institute of Pathology, Charite University Medicine Berlin, D-10117 Berlin, Germany; §Department of Stem Cell Therapy Science, Graduate School of Medicine, Osaka University, Suita, Osaka 565-0871, Japan; ¶Institute for Oral Sciences, Matsumoto Dental University, Shiojiri, Nagano 399-0871, Japan; ‖Planning & Development Group, Bioindustry Division, Oriental Yeast Co., Itabashi-ku, Tokyo 174-8505, Japan; #Laboratory for Cell Function and Dynamics, Brain Science Institute, RIKEN, Wako City, Saitama 351-0198, Japan; **Laboratory for Autoimmune Regulation, Research Center for Allergy and Immunology, RIKEN, Tsurumi, Yokohama City, Kanagawa 230-0045, Japan; and ††Center for Innovation in Immunoregulative Technology and Therapeutics, Graduate School of Medicine, Kyoto University, Yoshidakonoe-cho, Sakyo-ku, Kyoto 606-8051, Japan

Received for publication May 11, 2012. Accepted for publication November 15, 2012.

This work was supported by Grants-in-Aid for Encouragement of Young Scientists (A) (22689030 to M.I.) and for Scientific Research on Innovative Areas (22113007 to M.I.; 23113506 to M.T.) and by a Funding Program for World-Leading Innovative R&D on Science and Technology (FIRST Program) (to M.I.) from the Ministry of Education, Science, Sports and Culture of Japan; by a Grant-in-Aid for Research on Allergic Disease and Immunology (H21-010 to M.I.) from the Ministry of Health, Labor and Welfare of Japan; grants from the International Human Frontier Science Program (CDA-00059/2009 and RGY0077/2011 to M.I.); and by grants from the Takeda Science Foundation (to M.I.), the Cell Science Research Foundation (to M.I.), the Astellas Foundation for Research on Metabolic Disorders (to M.I.), the Nakajima Foundation (to M.I.), and the Sumitomo Science Foundation (to M.T.).

Address correspondence and reprint requests to Prof. Masaru Ishii, Laboratory of Cellular Dynamics, WPI-Immunology Frontier Research Center, Osaka University, 3-1 Yamada-oka, Suita, Osaka 565-0871, Japan. E-mail address: mishii@ifrec.osaka-u.ac.jp

The online version of this article contains supplemental material.

Abbreviations used in this article: BV/TV, bone volume/tissue volume; KikGR, Kikume Green-Red protein; RANK, receptor activator for NF-κB; RANKL, receptor activator for NF-κB ligand; S1P, sphingosine-1-phosphate; TRAP, tartrate-resistant acid phosphate.

www.jimmunol.org/cgi/doi/10.4049/jimmunol.1201345

In the current study, to investigate whether circulating osteoclast precursors have the potential to differentiate into osteoclasts, we used two different experimental methods: a shared blood circulation "parabiosis" system (16, 17) and photoconversion-based cell tracking with a Kikume Green-Red protein (KikGR). Parabiosis enables one to determine whether cells/molecules are circulating or not (16–18). KikGR is a photoconvertible GFP cloned from the coral *Favia favus* whose emission changes from green to red upon exposure to violet light (19). We generated monocyte/osteoclast ($RANK^+$)-specific KikGR-expressing mice, and cells in the spleen were marked by photoconversion to determine whether they can migrate to bones and differentiate into mature osteoclasts. These novel approaches using fluorescence imaging techniques are useful for tracking cellular dynamics in vivo (20–22).

Materials and Methods

Mice

CX_3CR1-EGFP knock-in mice (23) were obtained from The Jackson Laboratory (Bar Harbor, ME). RANK-Cre knock-in mice were generated as previously reported (24). The ROSA-CAG-lox-stop-lox-KikGR knock-in mice were generated at RIKEN and are described elsewhere (M. Tomura, A. Miyawaki, and O. Kanagawa, manuscript in preparation). These two strains were crossed to generate RANK promoter-driven KikGR-expressing mice (RANK-KikGR). All mice were bred and maintained under specific pathogen–free conditions at the animal facilities of Osaka University, and all animal experiments were performed according to Osaka University animal experiment guidelines using approved protocols.

Parabiosis

Parabiotic surgery was performed according to a previously published protocol (25). A CX_3CR1-EGFP knock-in mouse was surgically joined to a wild-type mouse. The two mice were housed together in a single cage for 1 wk preoperatively. At age 8 wk, the mice were anesthetized with isoflurane (Escain; Mylan, Canonsburg, PA). The dorsal and lateral aspects of each mouse were shaved and treated with hair-removal lotion (Epilat; Kracie Holdings, Tokyo, Japan). Matching skin incisions were made from the shoulder to the knee joint of each mouse. Approximate 1-cm incisions in the peritoneum were made in each mouse, and the mice were attached using 3-0 coated Vicryl (Ethicon, Somerville, NJ). Next, the dorsal and ventral skin was stitched through continuous suture, and the matching skin was sterilized using Isodine 10% solution (Meiji Seika Pharma, Tokyo, Japan). To ensure the animals' well-being for 4 wk, individual parabiotic mouse pairs were placed in clean cages, and food pellets were provided on the floor to minimize the strain of reaching for food while adjusting to parabiotic existence. Established shared blood circulation was confirmed by injection of Evans blue dye (Tokyo Chemical Industry, Tokyo, Japan). A total of 200 μl 0.5% Evans blue dye in saline was injected intravenously into the sides of CX_3CR1-EGFP knock-in mice.

Receptor activator for NF-κB ligand (RANKL) and FTY720 treatment

FTY720 (Cayman Chemical, Ann Arbor, MI) was dissolved in DMSO (Nacalai Tesque, Kyoto, Japan). FTY720 solution was diluted in saline containing 30% fatty acid–free BSA (Sigma-Aldrich, St. Louis, MO) (5% FTY720 solution). Parabiotic pairs were injected i.p. with FTY720 solution for 3 d (3 mg/kg body weight) and GST-RANKL (Oriental Yeast, Tokyo, Japan) (20 μg/pair) dissolved in saline for 2 d. RANKL-treated mice received vehicle (5% DMSO, 30% fatty acid–free BSA in saline) for 3 d and RANKL (20 μg/pair) for 2 d. The mice were sacrificed 48 h after the last injection, and the femurs were harvested and analyzed by bone histomorphometry and immunofluorescence analysis.

Photoconversion

Single-cell suspensions of splenocytes were exposed to violet light (200 mW/cm^2) with a 436-nm g-line band-pass filter using spot UV curing equipment (SP500; Usio, Tokyo, Japan). For spleen photoconversion, RANK-KikGR mice were anesthetized with isoflurane, and their fur was removed with an electric shaver. A midline incision was made in the abdominal skin to expose the spleen. The surrounding tissue was covered with aluminum foil to prevent unnecessary exposure, and then the spleen was exposed to violet light (200 mW/cm^2) with a 436-nm g-line band-pass filter with spot UV curing equipment. The three sides of the spleen were exposed for 10 min. The wound was closed with suture, and the matching skin was sterilized using Isodine 10%.

Flow cytometry analysis

Cells were washed with staining buffer [2% FBS and 0.03% sodium azide (both from Sigma-Aldrich) in saline]. The fluorescent cells were analyzed using a FACSCanto flow cytometer (BD Biosciences, Franklin Lakes, NJ). Data were analyzed using FlowJo software (Tree Star, Ashland, OR).

Immunofluorescence analysis

Femurs were removed and fixed through incubation overnight with 4% paraformaldehyde (Sigma-Aldrich) in 0.1 M phosphate buffer. The samples were frozen in chilled hexane (Wako, Osaka, Japan) using dry ice. Then, sections (10 μm thick) of nondecalcified femur were prepared using a Multi-Purpose Cryosection Preparation Kit (Section-Lab, Hiroshima, Japan, and Leica Microsystems, Wetzlar, Germany) (26). The sections were subjected to fluorescence-based staining for tartrate-resistant acid phosphate (TRAP) using ELF97 substrate (Life Technologies, Carlsbad, CA). The samples were observed using a TCS-SP5 confocal microscope (Leica Microsystems) and were illuminated with a laser (wavelength: 405 nm for ELF97, 488 nm for EGFP and Green KikGR, and 561 nm for Red KikGR). Collagen-enriched bone matrices were visualized by the second harmonic emission from collagen fibers excited with infrared lasers. The sections were examined using a TCS-SP5 multiphoton laser microscope (Leica Microsystems) (wavelength 880 nm) driven by a Chameleon XR Sapphire laser (Coherent, Santa Clara, CA). Emission signals were obtained by setting the wavelength to 500–575 nm for ELF97, 500–550 nm for EGFP and Green KikGR, 575–625 nm for Red KikGR, and 430–450 nm for the second harmonic emission. Image analysis was performed using a fully automated, high-throughput method to measure the interface between trabecular bone and osteoclasts (14, 27). The "$EGFP^+$ $TRAP^+$ osteoclasts/total $TRAP^+$ osteoclasts" ratio was calculated without manual intervention. An $EGFP^+$ $TRAP^+$ osteoclast indicated 25% of the area of an EGFP signal in a $TRAP^+$ osteoclast. Threshold selection was optimized computationally.

Bone histomorphometry

Trabecular bone morphometry within the metaphyseal region of the distal femur was quantified by micro-CT (ScanXmate-RX; Comscantechno, Kanagawa, Japan). Three-dimensional microstructural image data were reconstructed, and bone volume/tissue volume (BV/TV; %) ratio was calculated using TRI/3D-BON software (RATOC Systems, Tokyo, Japan). Bone morphometric analysis was performed as described previously (28).

Quantitative RT-PCR analysis

Total RNA and cDNA were prepared using a NucleoSpin RNA XS kit (TaKaRa, Shiga, Japan) and Superscript III reverse transcriptase (Life Technologies) according to the manufacturers' instructions. Real-time PCR analysis was performed with a Thermal Cycler Dice Real Time system (TaKaRa) using SYBR Premix EX Taq (Tli RNaseH Plus) (TaKaRa). Gene expression values were calculated by the ΔΔCt method using Gapdh as an internal control. The following primers were used: Rank, 5′-TCCCGACCCAGAGATATCAGAAG-3′ and 5′-CAGTCGGGATCAGTGTGAGGA-3′; and Gapdh, 5′-ACCACAGTCCATGCCATCAC-3′ and 5′-TCCACCACCCTGTTGCTGTA-3′. The Rank primer sequences were obtained using the Perfect Real-Time support system (TaKaRa).

Cell culture

To obtain osteoclast-like cells in vitro, bone marrow cells were obtained from the femurs and tibiae of C57BL/6J mice, and 5×10^4 of these were cultured for 48 h in 96-well plates in α-MEM (MP Biomedicals, Solon, OH) containing 10% FBS and 10 ng/ml human M-CSF (R&D Systems, Minneapolis, MN). Then the cells were cultured for 3 d in fresh medium containing 10 ng/ml human M-CSF and 50 ng/ml human RANKL (PeproTech, Rocky Hill, NJ). After being cultured for 5 d, the cells were fixed with 4% paraformaldehyde in 0.1 M PB and stained for TRAP (4, 5).

Statistical analysis

The Mann–Whitney rank sum test was performed using GraphPad PRISM software (GraphPad Software, La Jolla, CA) to calculate p values for highly skewed distributions. For Gaussian-like distributions, two-tailed t tests were used.

Distribution of materials

ROSA-CAG-lox-stop-lox-KikGR knock-in mice will be distributed from the RIKEN Bio-Resource Center Experimental Animal Division (http://www.brc.riken.go.jp/lab/animal/en/).

Results

Establishment of cross-blood circulation "parabiosis"

We generated parabiosis mouse pairs with heterozygous CX_3CR1-EGFP knock-in and wild-type mice. Because the chemokine receptor CX_3CR1 is known to be expressed in monocytoid cells, including osteoclast precursors (29), we were able to track the movement of osteoclast precursors between paired mice via the blood circulation. We showed by flow cytometry that 3.93 ± 0.71% (mean ± SEM; $n = 3$) of all bone marrow cells in CX_3CR1-EGFP knock-in mice were $EGFP^+$ (Fig. 1A). Such cells have been reported to readily differentiate into mature osteoclasts in vitro (15). We also showed that most of the mature $TRAP^+$ osteoclasts in these mice expressed EGFP (Fig. 1Bd). Further, we confirmed that CX_3CR1-$EGFP^+$ cells could efficiently differentiate into mature osteoclast-like cells and have potency for resorbing bone tissues (dentin slices) in vitro (Supplemental Fig. 1). These results confirmed that $EGFP^+$ cells include osteoclast precursors. Four weeks after surgery, we checked the sharing of blood circulation between the paired mice by i.v. injection of 0.5% Evans blue dye in one side (data not shown). Flow cytometric analyses showed that $EGFP^+$ cells were present in the bone marrow of the wild-type mice. These monocytes, which included osteoclast precursors, had migrated from CX_3CR1-EGFP knock-in mice via the bloodstream (Fig. 1C). The percentage of $EGFP^+$ cells in wild-type mice [0.32 ± 0.09% (mean ± SEM), $n = 3$] was smaller than that in the joined CX_3CR1-EGFP knock-in mice (Fig. 1A). These results suggested that substantial numbers of CX_3CR1^+ osteoclast precursors from wild-type mice remained without repopulation in the wild-type bone marrow, and recruitment and homing of monocytes into bone marrow tissues limited the number of $EGFP^+$ osteoclast precursors in wild-type mice. We also checked sections of bone from joined wild-type mice (Fig. 1D). We detected mature $EGFP^+$ $TRAP^+$ osteoclasts lining the bone trabeculae (Fig. 1Dd, arrowhead), as well as $TRAP^+$ osteoclasts (Fig. 1Dd, asterisks). We confirmed that $EGFP^+$ osteoclasts originating from circulating precursors were localized along the eroded bone surface and participated in active bone resorption (data not shown). These results clearly suggest that circulating CX_3CR1-$EGFP^+$ osteoclast precursors could home to bone surfaces and differentiate into mature osteoclasts in situ.

The dynamic nature of osteoclast precursor migration

Next, we examined whether the mobilization of circulating osteoclast precursors was affected by bone-resorptive conditions. Intraperitoneal injection of recombinant RANKL has been shown to enhance osteoclastic bone resorption and potently to induce osteopenia (30). After establishment of a shared blood circulation, RANKL (20 μg/pair) or saline (control) was administered in 24-h intervals for 2 d to the sides of wild-type mice. The jointed pairs were killed 24 h after the last injection. In wild-type mice, bone mineral density, defined as the BV/TV ratio (%), was significantly reduced by application of RANKL (Fig. 2A, 2B).

To evaluate the contribution of circulating $EGFP^+$ osteoclast precursors to RANKL-induced osteoclastogenesis, we first checked the number of $EGFP^+$ cells in the bone marrow of wild-type mice. The number of $EGFP^+$ cells was increased by RANKL treatment, indicating the increased recruitment of precursor monocytes into the bone marrow cavity (Fig. 2C). Next, we performed immunofluorescence analysis of sections of bone from control and RANKL-treated wild-type mice from the mouse pairs (Fig. 2D). Fluorescent image data were automatically processed as described in the *Materials and Methods* section to quantify objectively the proportion of $TRAP^+$ osteoclasts that were also positive for EGFP; the proportion was significantly increased by RANKL application (Fig. 2E), indicating that the contribution of circulating precursors to osteoclast formation on the endosteum was increased under these conditions (Fig. 2F). These results suggest that sources of osteoclast precursors may change in association with several pathological bone conditions, including bone-resorptive disorders.

Next, we checked the effect of the S1P receptor agonist FTY720 on the proportion of osteoclasts that were $EGFP^+$. As shown previously, migration of osteoclast precursors was regulated by blood S1P, and application of FTY720 may facilitate the recirculation of osteoclast precursors from bone to blood and thereby

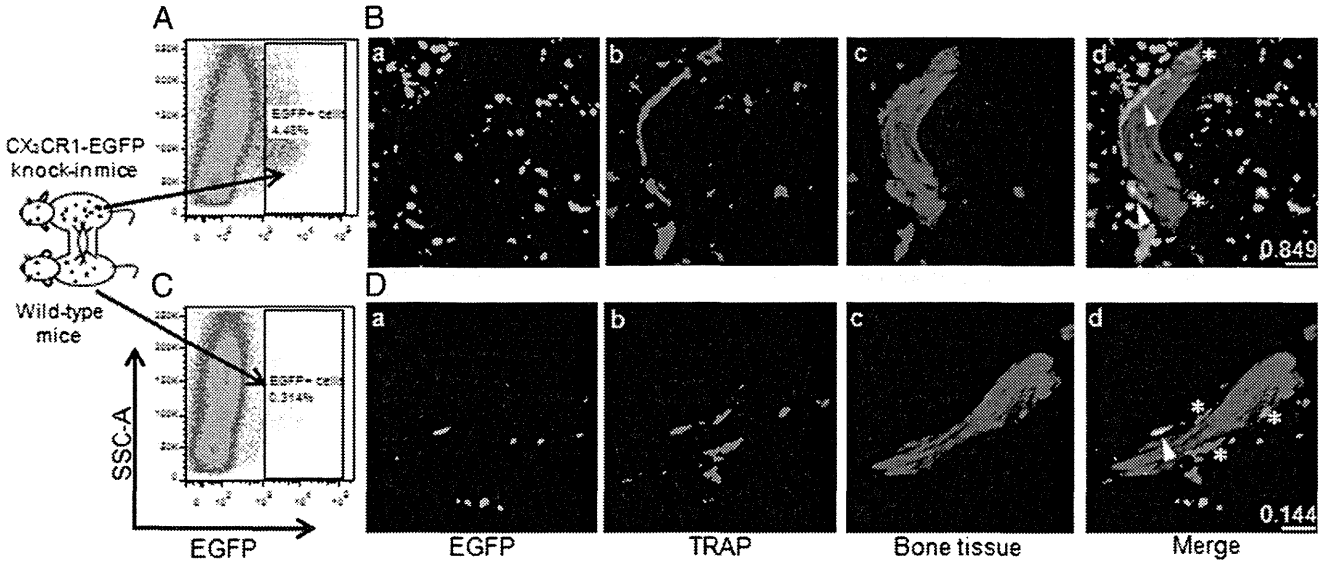

FIGURE 1. Generation of shared blood circulation in parabiotic animals. (**A** and **C**) Flow cytometric analysis of bone marrow cells from CX_3CR1-EGFP knock-in mice (A) and wild-type mice (C). Bone marrow cells were analyzed for EGFP expression. Three pairs of animals were independently analyzed and gave similar results. The results of one representative analysis are shown. (**B** and **D**) Femoral bone tissues from CX_3CR1-EGFP knock-in mice (B) and wild-type mice (D). Images of EGFP fluorescence (**a**), TRAP staining (**b**), second harmonic generation of bone tissue (**c**), and overlay with a transmission image (**d**). Arrowhead, mature $EGFP^+$ $TRAP^+$ osteoclast; asterisks, mature $TRAP^+$ osteoclasts. The $EGFP^+$ $TRAP^+$ osteoclast/total $TRAP^+$ osteoclast ratios are indicated by the white numbers in the *bottom right corners*. Scale bars, 30 μm.

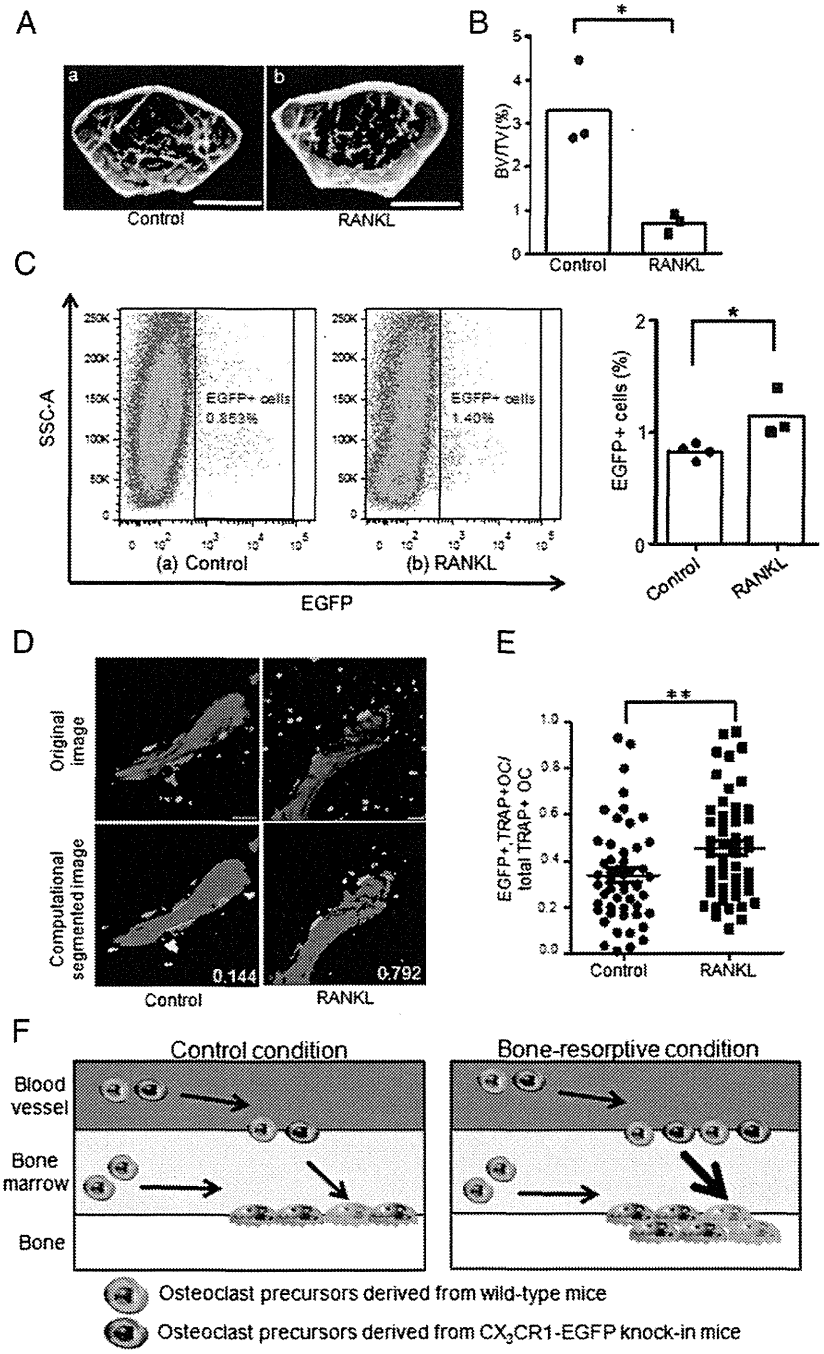

FIGURE 2. *Mobilization of circulating osteoclast precursors under bone-resorptive conditions.* (**A**) Characterization of the RANKL-induced bone loss model. Femurs were collected from wild-type mice after RANKL was i.p. injected (20 μg/pair) for 2 d (**b**). Control parabiotic pairs were injected with saline only (**a**). Scale bars, 1 mm. (**B**) Bone samples were measured by cone-beam μCT. BV/TV (%) was calculated from μCT images. $*p < 0.05$ (two-tailed unpaired t test). (**C**) Flow cytometric analyses of bone marrow cells collected from wild-type mice connected with CX_3CR1-EGFP knock-in mice after i.p. injection of saline (**a**) or RANKL (**b**) ($n = 4$ and $n = 3$, respectively). $*p < 0.05$ (two-tailed unpaired t test). (**D**) Histological examination combined with computational analysis to measure the length of the white line. *Upper panels*, original images; *lower panels*, segmented images. Blue area, bone trabeculae (second harmonic fluorescent signal); orange and yellow area, $EGFP^+$ $TRAP^+$ osteoclasts attached to or detached from bone trabeculae, respectively; red and green area, $TRAP^+$ osteoclasts attached to or detached from bone trabeculae; white line, osteoclast and bone attachment interface. The $EGFP^+$ $TRAP^+$ osteoclast/total $TRAP^+$ osteoclast ratios are indicated by white numbers. Scale bars, 30 μm. (**E**) Proportion of $TRAP^+$ osteoclasts that were $EGFP^+$. Data represent the mean ± SEM ($n = 52$). $**p < 0.01$ (two-tailed unpaired t test). (**F**) Schematic illustration of osteoclast precursor mobilization. Osteoclast precursors can be generated from circulating monocytes (green + gray), as well as bone-resident precursors (gray). Under bone-resorptive conditions, recruitment of circulating monocytes into bones is increased, leading to an increase in proportion of osteoclasts on the bone surface that are positive for EGFP (green).

prevent loss of bone density during ovariectomy-induced osteoporosis (14). We induced osteoclastic bone resorption in parabiotic mouse pairs through i.p. injection of RANKL (20 μg/pair) and further administered FTY720 (3 mg/kg) or vehicle in 24-h intervals to test their therapeutic effects (Fig. 3A). The jointed pairs were killed 48 h after the last injection, and we confirmed that the bone mineral density, defined as the BV/TV ratio (%), was significantly increased in FTY720-treated wild-type mice (Fig. 3B), as observed in the ovariectomy model (14). We also demonstrated that the total number of $EGFP^+$ cells in bone marrow was significantly decreased by FTY720 treatment (Fig. 3C), which is also consistent with the literature (14).

We performed immunofluorescence analysis of bone sections from mice treated with RANKL with or without FTY720 (Fig. 3D). Although the total number of bone-lining osteoclasts was significantly decreased in mice treated with FTY720 (14), the proportion of osteoclasts that were $EGFP^+$ did not differ significantly between the two groups (Fig. 3E). These results suggest that $EGFP^-$ osteoclast precursors generated in wild-type bone marrow and $EGFP^+$ precursors originally derived from CX_3CR1-EGFP knock-in mouse bones and homed into wild-type bone marrow have comparable abilities to recirculate into the bloodstream after application of FTY720. However, we could not completely exclude the possibility that FTY720 may influence the differentiation of osteoclasts (Fig. 3F).

Tracking the movement of osteoclast precursors in photoconvertible fluorescence protein "KikGR" knock-in mice

To clarify whether osteoclast precursors were really circulating, we also used a different technique involving the photoconvertible fluorescent protein KikGR. We applied this method to study dynamic cell behavior using mouse strains in which KikGR is

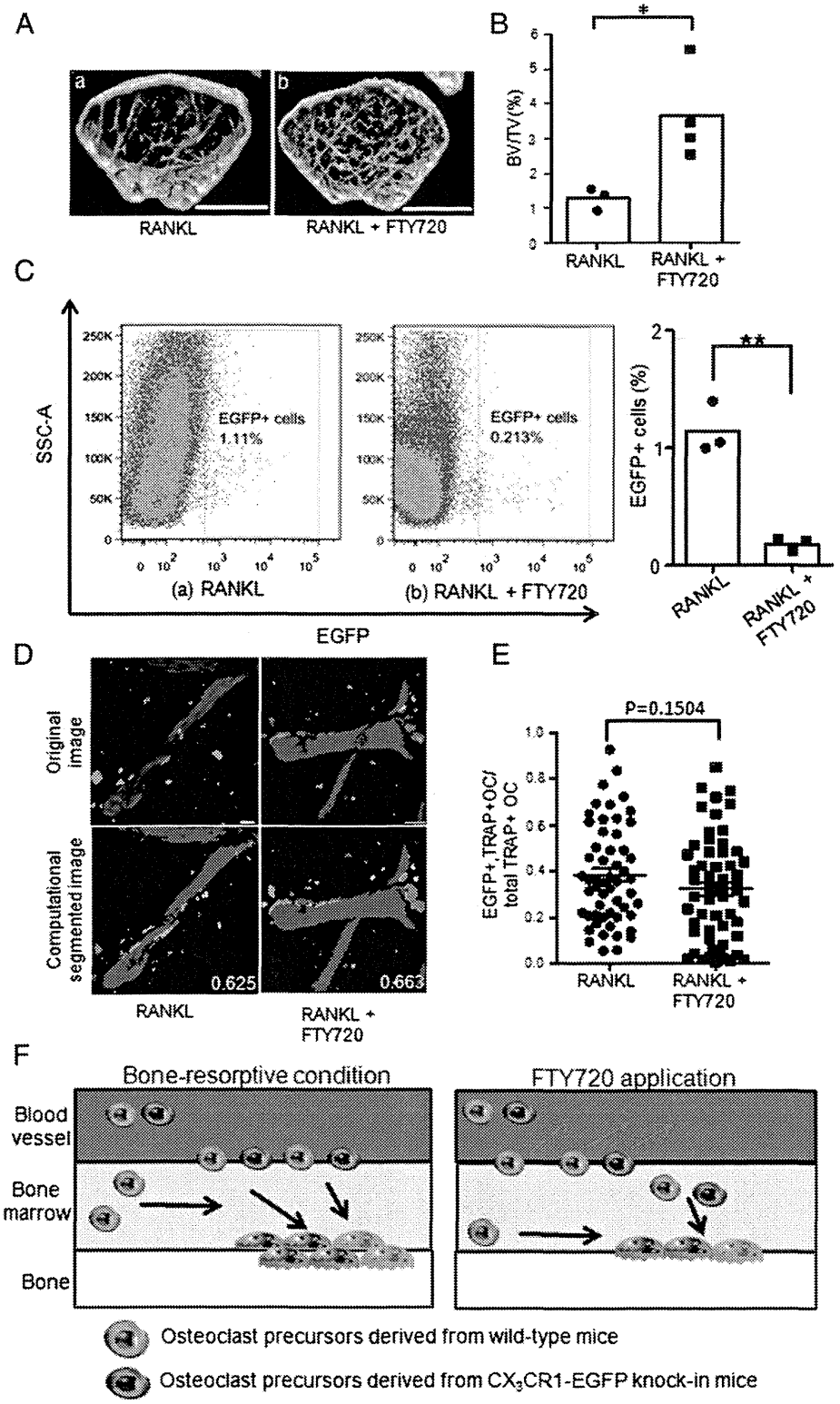

FIGURE 3. Mobilization of circulating osteoclast precursors under bone-treatment conditions. (**A**) Characterization of the effect of FTY720 administration. Femurs were collected from wild-type mice after i.p. injection of RANKL + vehicle ($n = 3$) (**a**). FTY720-treated parabiotic pairs were injected with RANKL + FTY720 ($n = 4$) (**b**). Scale bars, 1 mm. (**B**) Bone samples were analyzed by cone-beam μCT. BV/TV (%) was calculated from μCT images. $^*p < 0.05$ (two-tailed unpaired t test). (**C**) Flow cytometric analyses of bone marrow cells collected from RANKL-treated (**a**) and RANKL + FTY720-treated (**b**) mice ($n = 3$). $^{**}p < 0.01$ (two-tailed unpaired t test). (**D**) Histological examination combined with computational analysis to measure the length of the white line. *Upper panels*, original images; *lower panels*, computational segmented images. The EGFP$^+$ TRAP$^+$ osteoclast/total TRAP$^+$ osteoclast ratios are indicated by white numbers. Scale bars, 30 μm. (**E**) Proportion of TRAP$^+$ osteoclasts that were EGFP$^+$. Data represent the mean ± SEM ($n = 55$ for RANKL and $n = 58$ for RANKL + FTY720). (**F**) Schematic illustration of FTY720-induced recirculation of osteoclast precursors. Osteoclast precursors can be generated from circulating monocytes (green + gray), as well as bone-resident precursors (gray). After FTY720 treatment, both green and gray osteoclast precursors are equally able to recirculate into the bloodstream, resulting in the proportion of osteoclasts that are positive for EGFP (green) being unaltered.

expressed in osteoclast precursors. We generated RANK-KikGR mice by crossing ROSA-CAG-lox-stop-lox-KikGR knock-in mice with RANK-Cre knock-in mice. RANK is a cognate receptor for RANKL, which is required for differentiation into mature osteoclasts (31). Bone marrow cells from RANK-KikGR mice were analyzed by flow cytometry (Fig. 4A). We confirmed that 0.659 ± 0.16% (mean ± SEM; $n = 3$) of all bone marrow cells expressed KikGR, and that KikGR$^+$ cells could differentiate into TRAP$^+$ osteoclast-like cells in vitro (Fig. 4B). Furthermore, Rank mRNA expression was higher in KikGR$^+$ cells than in KikGR$^-$ cells (Fig. 4C), indicating that some KikGR$^+$ cells in RANK-KikGR mice are osteoclast precursors.

We evaluated the efficiency of photoconversion of KikGR expressed in RANK$^+$ cells in single-cell suspensions. Splenocytes from RANK-KikGR mice exposed to violet light (436 nm) for 10 min exhibited red-shifted emission signals compared with non-exposed cells (Fig. 4D), indicating successful photoconversion under this condition. Next, we assessed the photoconversion ef-

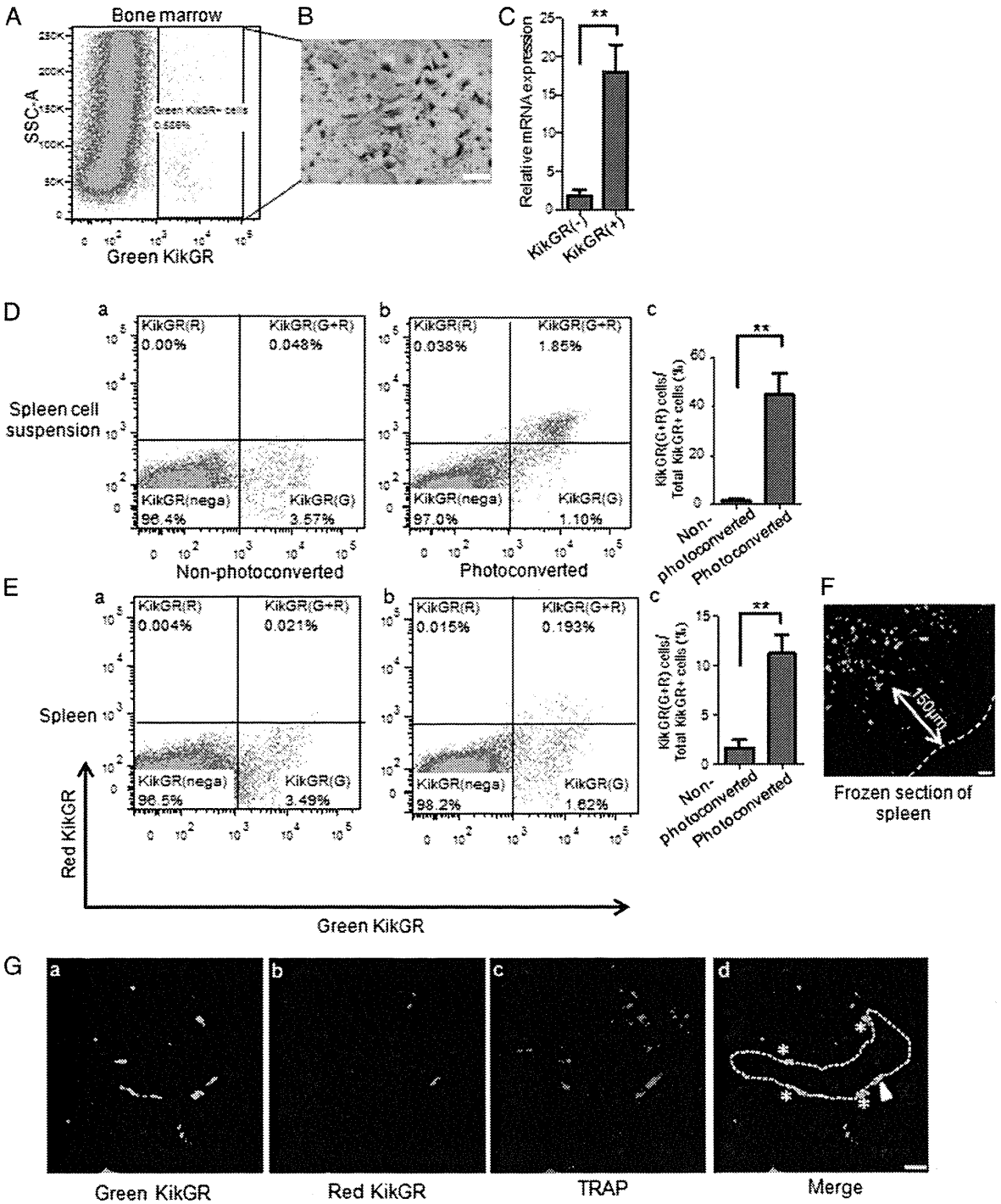

FIGURE 4. Tracking the circulation of osteoclast precursors in KikGR transgenic mice in vivo. (**A**) Separation of the KikGR$^+$ cell population by flow cytometry. (**B**) Representative images of TRAP$^+$ osteoclast-like cells generated from KikGR$^+$ cells cultured with M-CSF (10 ng/ml) and RANKL (50 ng/ml). Scale bar, 200 μm. (**C**) Real-time quantitative PCR analysis of mRNA for Rank expression in KikGR$^+$ cells and KikGR$^-$ cells. Data represent the mean ± SEM (n = 3). (**D**) Flow cytometric analysis of non-photoconverted (**a**) and photoconverted (**b**) spleen cells. (**E**) Spleens were exposed as described in the *Materials and Methods* section, and wounds were closed surgically on day 0 (**b**). Non-photoconverted spleen cells are shown as a control (**a**). (D and E) The corresponding proportions of red KikGR$^+$ cells are shown (**c**). Data represent the mean ± SEM Three animals were independently analyzed. (**F**) Frozen spleen sections were visualized by confocal microscopy immediately after violet light irradiation. Scale bar, 30 μm. (**G**) Femoral bone tissues. Fluorescence image of green KikGR (**a**), fluorescence image of red KikGR (**b**), staining for TRAP (**c**), and overlay with a transmission image (**d**). Arrowhead, green and red mature KikGR$^+$ osteoclast; asterisks, green mature KikGR$^+$ osteoclasts. Scale bar, 30 μm. $^{**}p < 0.01$ (two-tailed unpaired t test).

ficiency in the spleen after exposure to violet light in situ. Spleens were accessed by making small incisions in the skin and were exposed to violet light (436 nm). A total of 11.28 ± 1.90% (mean ± SEM; n = 3) of KikGR in these cells was photoconverted and showed shifts in emission spectra (Fig. 4E). Histological examination of spleens showed that only KikGR-expressing cells near the surface of the spleen could be photoconverted (Fig. 4F), which explains the low efficiency compared with single-cell suspension.

Under bone-resorptive conditions induced by the application of RANKL, we detected a small number of mature TRAP$^+$ osteoclasts

that expressed red (photoconverted) KikGR (Fig. 4G). This result clearly demonstrates that osteoclast precursors from the spleen migrated to the bone marrow and differentiated into mature osteoclasts during these 2 d.

Discussion

Using two different experimental methods, we clearly demonstrated that circulating monocytoid precursors are capable of differentiating into osteoclasts, although we think that osteoclasts can also be derived from precursors within the same bone marrow cavity. We showed that some osteoclast precursors exit the bone marrow after they have been produced by hematopoiesis, circulate via the bloodstream, and enter the bone spaces that need to be resorbed. What is the relevance of this detour for osteoclast formation? Bone resorption does not occur homogeneously in all bone tissues (32). This implies that the site of bone resorption is not necessarily the same as that of osteoclast precursor generation. The most extreme example is bone destruction in arthritic joints, such as in fingers, where hematopoiesis is not so dominant. The versatile circulation system of monocytoid precursors would be reasonable and beneficial for delivering osteoclast precursors from their site of origin to the site that actually needs bone destruction (33). More importantly, we showed that the recruitment of circulating precursor monocytes into the bone marrow cavity was enhanced by bone-resorptive states, such as that induced by RANKL treatment. These results suggest that unknown mechanisms control precursor recruitment in a RANKL-dependent manner. In this regard, we have to be aware that parabiotic mice were under conditions of slightly increased bone resorption because of their restricted motion, as observed in the tail suspension model (34). Fewer circulating precursor monocytes may be recruited under more physiological (nonparabiotic) conditions (Supplemental Fig. 2).

The system presented shows marked differences from the development of other monocytoid cells such as microglia, which are essentially derived from primordial tissue-resident precursors (11). We also found that no $EGFP^+$ microglia could be detected in the brain of the wild-type mice of the parabiotic pairs, whereas small numbers of dermal dendritic cells and liver Kupffer cells were $EGFP^+$ (data not shown). These results suggest that different types of monocytoid cells have intrinsic modes of precursor cell recruitment in situ.

The molecular mechanisms of egress and entry of circulating osteoclast precursors from and to the bone marrow remain to be elucidated. Several chemokines and lipid mediators, including SDF-1/CXCL12 and S1P, have been reported to be involved in osteoclast precursor localization (6, 7). Now that osteoclast precursors have been clearly shown to circulate in the body, we may consider a novel line of therapy for bone-resorptive diseases that targets the migratory behavior of osteoclast precursors. Most anti–bone resorption drugs, including bisphosphonates, target mature osteoclasts (35). The new therapeutic approach proposed in this study has completely different pharmacological properties and may be promising for future drug discoveries in this field.

Acknowledgments

We thank Dr. Satoshi Ueha (The University of Tokyo) for helpful discussion regarding the analyses on the mobilization of circulating monocytes. We also thank Mai Shirazaki and Masami Kasaoka (Osaka University) for technical assistance.

Disclosures

The authors have no financial conflicts of interest.

References

1. Teitelbaum, S. L., and F. P. Ross. 2003. Genetic regulation of osteoclast development and function. *Nat. Rev. Genet.* 4: 638–649.
2. Xing, L., E. M. Schwarz, and B. F. Boyce. 2005. Osteoclast precursors, RANKL/RANK, and immunology. *Immunol. Rev.* 208: 19–29.
3. Yao, Z., P. Li, Q. Zhang, E. M. Schwarz, P. Keng, A. Arbini, B. F. Boyce, and L. Xing. 2006. Tumor necrosis factor-alpha increases circulating osteoclast precursor numbers by promoting their proliferation and differentiation in the bone marrow through up-regulation of c-Fms expression. *J. Biol. Chem.* 281: 11846–11855.
4. Mizoguchi, T., A. Muto, N. Udagawa, A. Arai, T. Yamashita, A. Hosoya, T. Ninomiya, H. Nakamura, Y. Yamamoto, S. Kinugawa, et al. 2009. Identification of cell cycle-arrested quiescent osteoclast precursors in vivo. *J. Cell Biol.* 184: 541–554.
5. Muto, A., T. Mizoguchi, N. Udagawa, S. Ito, I. Kawahara, Y. Abiko, A. Arai, S. Harada, Y. Kobayashi, Y. Nakamichi, et al. 2011. Lineage-committed osteoclast precursors circulate in blood and settle down into bone. *J. Bone Miner. Res.* 26: 2978–2990.
6. Ishii, T., Y. Shimazu, I. Nishiyama, J. Kikuta, and M. Ishii. 2011. The role of sphingosine 1-phosphate in migration of osteoclast precursors; an application of intravital two-photon microscopy. *Mol. Cells* 31: 399–403.
7. Kollet, O., A. Dar, S. Shivtiel, A. Kalinkovich, K. Lapid, Y. Sztainberg, M. Tesio, R. M. Samstein, P. Goichberg, A. Spiegel, et al. 2006. Osteoclasts degrade endosteal components and promote mobilization of hematopoietic progenitor cells. *Nat. Med.* 12: 657–664.
8. Cambier, J. C., S. B. Gauld, K. T. Merrell, and B. J. Vilen. 2007. B-cell anergy: from transgenic models to naturally occurring anergic B cells? *Nat. Rev. Immunol.* 7: 633–643.
9. Berg, L. J. 2007. Signalling through TEC kinases regulates conventional versus innate CD8(+) T-cell development. *Nat. Rev. Immunol.* 7: 479–485.
10. Merad, M., M. G. Manz, H. Karsunky, A. Wagers, W. Peters, I. Charo, I. L. Weissman, J. G. Cyster, and E. G. Engleman. 2002. Langerhans cells renew in the skin throughout life under steady-state conditions. *Nat. Immunol.* 3: 1135–1141.
11. Ginhoux, F., M. Greter, M. Leboeuf, S. Nandi, P. See, S. Gokhan, M. F. Mehler, S. J. Conway, L. G. Ng, E. R. Stanley, et al. 2010. Fate mapping analysis reveals that adult microglia derive from primitive macrophages. *Science* 330: 841–845.
12. Flügel, A., M. Bradl, G. W. Kreutzberg, and M. B. Graeber. 2001. Transformation of donor-derived bone marrow precursors into host microglia during autoimmune CNS inflammation and during the retrograde response to axotomy. *J. Neurosci. Res.* 66: 74–82.
13. Nagasawa, T. 2006. Microenvironmental niches in the bone marrow required for B-cell development. *Nat. Rev. Immunol.* 6: 107–116.
14. Ishii, M., J. G. Egen, F. Klauschen, M. Meier-Schellersheim, Y. Saeki, J. Vacher, R. L. Proia, and R. N. Germain. 2009. Sphingosine-1-phosphate mobilizes osteoclast precursors and regulates bone homeostasis. *Nature* 458: 524–528.
15. Ishii, M., J. Kikuta, Y. Shimazu, M. Meier-Schellersheim, and R. N. Germain. 2010. Chemorepulsion by blood S1P regulates osteoclast precursor mobilization and bone remodeling in vivo. *J. Exp. Med.* 207: 2793–2798.
16. Boban, I., C. Jacquin, K. Prior, T. Barisic-Dujmovic, P. Maye, S. H. Clark, and H. L. Aguila. 2006. The 3.6 kb DNA fragment from the rat Col1a1 gene promoter drives the expression of genes in both osteoblast and osteoclast lineage cells. *Bone* 39: 1302–1312.
17. Boban, I., T. Barisic-Dujmovic, and S. H. Clark. 2010. Parabiosis model does not show presence of circulating osteoprogenitor cells. *Genesis* 48: 171–182.
18. Harris, R. B. 1999. Parabiosis between db/db and ob/ob or db/+ mice. *Endocrinology* 140: 138–145.
19. Tsutsui, H., S. Karasawa, H. Shimizu, N. Nukina, and A. Miyawaki. 2005. Semi-rational engineering of a coral fluorescent protein into an efficient highlighter. *EMBO Rep.* 6: 233–238.
20. Tomura, M., N. Yoshida, J. Tanaka, S. Karasawa, Y. Miwa, A. Miyawaki, and O. Kanagawa. 2008. Monitoring cellular movement in vivo with photoconvertible fluorescence protein "Kaede" transgenic mice. *Proc. Natl. Acad. Sci. USA* 105: 10871–10876.
21. Tomura, M., T. Honda, H. Tanizaki, A. Otsuka, G. Egawa, Y. Tokura, H. Waldmann, S. Hori, J. G. Cyster, T. Watanabe, et al. 2010. Activated regulatory T cells are the major T cell type emigrating from the skin during a cutaneous immune response in mice. *J. Clin. Invest.* 120: 883–893.
22. Tomura, M., K. Itoh, and O. Kanagawa. 2010. Naive CD4+ T lymphocytes circulate through lymphoid organs to interact with endogenous antigens and upregulate their function. *J. Immunol.* 184: 4646–4653.
23. Jung, S., J. Aliberti, P. Graemmel, M. J. Sunshine, G. W. Kreutzberg, A. Sher, and D. R. Littman. 2000. Analysis of fractalkine receptor CX(3)CR1 function by targeted deletion and green fluorescent protein reporter gene insertion. *Mol. Cell. Biol.* 20: 4106–4114.
24. Maeda, K., Y. Kobayashi, N. Udagawa, S. Uehara, A. Ishihara, T. Mizoguchi, Y. Kikuchi, I. Takada, S. Kato, S. Kani, et al. 2012. Wnt5a-Ror2 signaling between osteoblast-lineage cells and osteoclast precursors enhances osteoclastogenesis. *Nat. Med.* 18: 405–412.
25. Jiang, Q., R. Oldenburg, S. Otsuru, A. E. Grand-Pierre, E. M. Horwitz, and J. Uitto. 2010. Parabiotic heterogenetic pairing of $Abcc6^{-/-}$/$Rag1^{-/-}$ mice and their wild-type counterparts halts ectopic mineralization in a murine model of pseudoxanthoma elasticum. *Am. J. Pathol.* 176: 1855–1862.
26. Kawamoto, T. 2003. Use of a new adhesive film for the preparation of multi-purpose fresh-frozen sections from hard tissues, whole-animals, insects and plants. *Arch. Histol. Cytol.* 66: 123–143.
27. Klauschen, F., M. Ishii, H. Qi, M. Bajénoff, J. G. Egen, R. N. Germain, and M. Meier-Schellersheim. 2009. Quantifying cellular interaction dynamics in 3D fluorescence microscopy data. *Nat. Protoc.* 4: 1305–1311.

28. Parfitt, A. M., M. K. Drezner, F. H. Glorieux, J. A. Kanis, H. Malluche, P. J. Meunier, S. M. Ott, and R. R. Recker; Report of the ASBMR Histomorphometry Nomenclature Committee. 1987. Bone histomorphometry: standardization of nomenclature, symbols, and units. *J. Bone Miner. Res.* 2: 595–610.
29. Koizumi, K., Y. Saitoh, T. Minami, N. Takeno, K. Tsuneyama, T. Miyahara, T. Nakayama, H. Sakurai, Y. Takano, M. Nishimura, et al. 2009. Role of CX3CL1/fractalkine in osteoclast differentiation and bone resorption. *J. Immunol.* 183: 7825–7831.
30. Tomimori, Y., K. Mori, M. Koide, Y. Nakamichi, T. Ninomiya, N. Udagawa, and H. Yasuda. 2009. Evaluation of pharmaceuticals with a novel 50-hour animal model of bone loss. *J. Bone Miner. Res.* 24: 1194–1205.
31. Nakagawa, N., M. Kinosaki, K. Yamaguchi, N. Shima, H. Yasuda, K. Yano, T. Morinaga, and K. Higashio. 1998. RANK is the essential signaling receptor for osteoclast differentiation factor in osteoclastogenesis. *Biochem. Biophys. Res. Commun.* 253: 395–400.
32. Aguirre, J. I., L. I. Plotkin, S. A. Stewart, R. S. Weinstein, A. M. Parfitt, S. C. Manolagas, and T. Bellido. 2006. Osteocyte apoptosis is induced by weightlessness in mice and precedes osteoclast recruitment and bone loss. *J. Bone Miner. Res.* 21: 605–615.
33. Danks, L., A. Sabokbar, R. Gundle, and N. A. Athanasou. 2002. Synovial macrophage-osteoclast differentiation in inflammatory arthritis. *Ann. Rheum. Dis.* 61: 916–921.
34. Amblard, D., M. H. Lafage-Proust, A. Laib, T. Thomas, P. Rüegsegger, C. Alexandre, and L. Vico. 2003. Tail suspension induces bone loss in skeletally mature mice in the C57BL/6J strain but not in the C3H/HeJ strain. *J. Bone Miner. Res.* 18: 561–569.
35. Reszka, A. A., and G. A. Rodan. 2003. Mechanism of action of bisphosphonates. *Curr. Osteoporos. Rep.* 1: 45–52.

Dynamic visualization of RANKL and Th17-mediated osteoclast function

Junichi Kikuta,[1,2] Yoh Wada,[3] Toshiyuki Kowada,[4] Ze Wang,[5] Ge-Hong Sun-Wada,[3] Issei Nishiyama,[1,2] Shin Mizukami,[4,6] Nobuhiko Maiya,[7] Hisataka Yasuda,[8] Atsushi Kumanogoh,[9] Kazuya Kikuchi,[4,6] Ronald N. Germain,[5] and Masaru Ishii[1,2]

[1]Laboratory of Cellular Dynamics, WPI–Immunology Frontier Research Center, Osaka University, Osaka, Japan. [2]Japan Science and Technology, CREST, Tokyo, Japan. [3]Division of Biological Sciences, Institute of Scientific and Industrial Research, and [4]Laboratory of Chemical Imaging Techniques, WPI–Immunology Frontier Research Center, Osaka University, Osaka, Japan. [5]Lymphocyte Biology Section, Laboratory of Systems Biology, National Institute of Allergy and Infectious Diseases, NIH, Bethesda, Maryland, USA. [6]Department of Material and Life Sciences, Graduate School of Engineering, Osaka University, Osaka, Japan. [7]Instruments Co., Nikon Corp., Kanagawa, Japan. [8]Planning and Development Group, Bioindustry Division, Oriental Yeast Co., Tokyo, Japan. [9]Department of Respiratory Medicine, Allergy and Rheumatic Disease, Graduate School of Medicine, Osaka University, Osaka, Japan.

Osteoclasts are bone resorbing, multinucleate cells that differentiate from mononuclear macrophage/monocyte-lineage hematopoietic precursor cells. Although previous studies have revealed important molecular signals, how the bone resorptive functions of such cells are controlled in vivo remains less well characterized. Here, we visualized fluorescently labeled mature osteoclasts in intact mouse bone tissues using intravital multiphoton microscopy. Within this mature population, we observed cells with distinct motility behaviors and function, with the relative proportion of static – bone resorptive (R) to moving – nonresorptive (N) varying in accordance with the pathophysiological conditions of the bone. We also found that rapid application of the osteoclast-activation factor RANKL converted many N osteoclasts to R, suggesting a novel point of action in RANKL-mediated control of mature osteoclast function. Furthermore, we showed that Th17 cells, a subset of RANKL-expressing CD4$^+$ T cells, could induce rapid N-to-R conversion of mature osteoclasts via cell-cell contact. These findings provide new insights into the activities of mature osteoclasts in situ and identify actions of RANKL-expressing Th17 cells in inflammatory bone destruction.

Introduction

Bone is a highly dynamic organ that is continuously being remodeled by the cooperative action of osteoclasts that resorb old bone and osteoblasts that create new bone. Osteoclasts are giant polykaryons differentiated from monocyte/macrophage-lineage hematopoietic precursor cells termed *osteoclast precursors*. Previous studies have revealed key molecular signals, such as those mediated by M-CSF and RANKL, which regulate the differentiation of these cells (1, 2). When cultured in the presence of M-CSF and RANKL, monocytoid cells isolated from bone marrow can successfully be differentiated into multinucleated giant cells in vitro, called *osteoclast-like cells*. However, the osteoclast-like cells generated in vitro often contain more than 100 nuclei (3), and it remains unclear whether such extraordinarily large polykaryons are formed in vivo, except in some pathological conditions such as Paget disease and giant cell tumors (4, 5). Furthermore, how the activity of multinucleate osteoclasts is controlled in vivo once they form remains largely unexplored. To address these issues and advance our understanding of this critical cell population with respect to bone homeostasis and osteopathology, we utilized intravital multiphoton microscopy (6–8).

Fully differentiated osteoclasts can adhere to bone surfaces and tightly seal the attachment areas with a characteristic membrane structure referred to as the "ruffled border" (Supplemental Figure 1A; supplemental material available online with this article; doi:10.1172/JCI65054DS1). A large number of vacuolar H$^+$-ATPases (V-type H$^+$-ATPases) are expressed along the ruffled border membrane in mature osteoclasts; these enzymes are responsible for secreting extraordinarily high numbers of protons, leading to acid resorption of the hard bone minerals (9, 10). V-type H$^+$-ATPase consists of multiple subunits, and each subunit has several isoforms; among them the a3 isoform of the *a* subunit is abundantly expressed in osteoclasts and is thus suitable as a marker for identifying mature osteoclasts (Supplemental Figure 1B and refs. 11, 12). In this study, by exploiting fluorescent reporter mice where GFP is expressed under the promoter of V-type H$^+$-ATPase a3 subunit (a3-GFP mice), we have succeeded in visualizing fluorescently labeled mature osteoclasts in live bones using intravital multiphoton microscopy. Based on such imaging, we have identified 2 different populations of mature osteoclasts in situ, corresponding with the static – bone resorptive (R) and moving – nonresorptive (N) fractions, with the transition between these states critically controlled by RANKL and showing a strong correlation to the state of cell motility. Our findings also revealed that RANKL-expressing Th17 regulates the status of mature osteoclasts by direct cell-cell contact, identifying what we believe is a novel mechanism of Th17-mediated inflammatory bone destruction.

Results

To label mature osteoclasts fluorescently, we modified the mouse *Tcirg1* locus, encoding the V-type H$^+$-ATPase a3 subunit, to produce a GFP fusion protein. Embryonic stem cell–mediated gene targeting was used to generate mice in which an a3 subunit-GFP fusion protein is expressed under the original promoter of the a3 subunit (a3-GFP mice) (13). Using bone tissue sections from these mice, we confirmed that tartrate-resistant acid phosphatase–positive (TRAP-positive) mature osteoclasts express GFP (Supplemental Figure 1C).

Conflict of interest: The authors have declared that no conflict of interest exists.
Citation for this article: *J Clin Invest.* doi:10.1172/JCI65054.

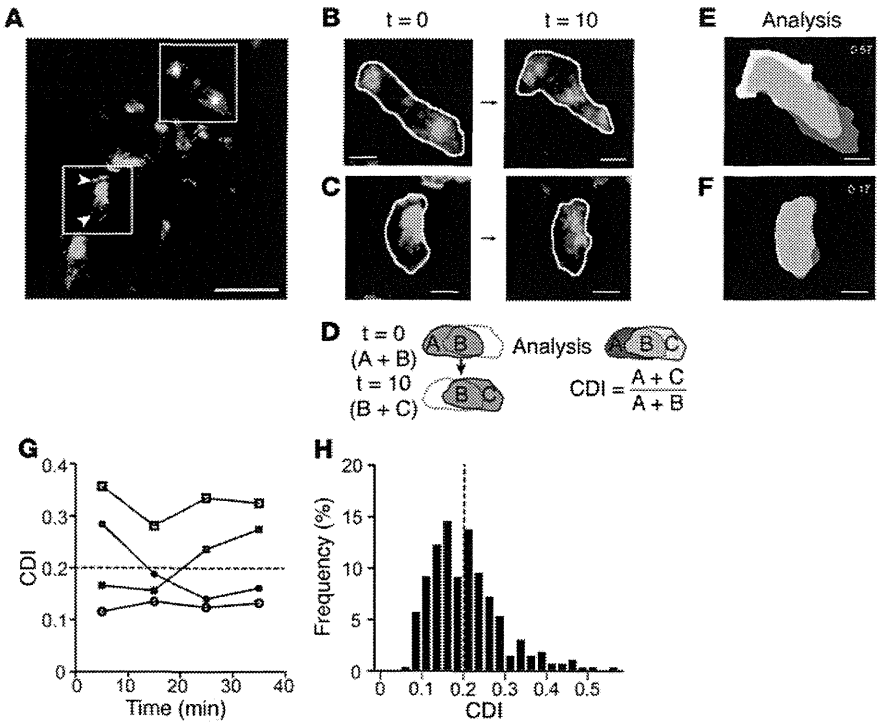

Figure 1
Visualization of living mature osteoclasts on the endosteum by using intravital multiphoton microscopy. (**A**) A representative image of live bone imaging of a3-GFP mice in control conditions. Green, mature osteoclasts expressing GFP-fused V-type H^+-ATPase a3 subunit; blue, bone surface. Scale bar: 40 μm. Arrowheads and asterisks represent surface and cytoplasmic distribution of V^-type H^+-ATPase a3 subunit, respectively. (**B** and **C**) Magnified images of 2 types of representative mature osteoclasts. White lines, cell borders. Scale bars: 10 μm. (**D**) Cell shapes were automatically recognized by the image analysis software, and 3 distinct areas were defined: occupied in the initial time frame (t = 0) (**A**, red), occupied in the final time frame (t = 10) (**C**, yellow), and overlapping between the 2 time frames (**B**, green). CDI was calculated as (A+C)/(A+B), representing the ratio of areas changed during 10 minutes divided by total cell area at t = 0 (see details in Supplemental Figure 2). (**E** and **F**) Processed images for CDI calculation (**E** for **B**, and **F** for **C**, respectively). Actual values of CDI were shown in upper right corners in **E** and **F**. Scale bars: 10 μm. (**G**) Examples of time-dependent transitions of CDIs. Each symbol represents a different cell tracked over a period of 40 minutes. Some cells changed their CDIs from lower to higher or vice versa (black symbols), whereas others remained in the similar CDI (white symbols). (**H**) Histogram of CDIs of mature osteoclasts under control conditions (n = 259, collected from 5 independent experiments).

By performing intravital multiphoton microscopy of calvaria in a3-GFP knockin mice, we could visualize live mature osteoclasts on the endosteum (Figure 1A and Supplemental Video 1). This live imaging identified a population of large multinuclear GFP^+ osteoclasts on the bone surface that showed substantial heterogeneity in terms of their amoeboid movements, including populations at the ends of a distribution of motilities that we could label as "moving" (Figure 1B) and "relatively static" (Figure 1C). These designations were derived from a quantitative analysis of osteoclast movement on the bone surface based on new image analysis software we developed for tracking the time-dependent morphological changes of these cells (Figure 1, D–F, Supplemental Figure 2, and Supplemental Video 2). Cell shapes were automatically recognized by the image analysis software before and after a certain period of time (10 minutes) (Supplemental Figure 2 and Supplemental Video 2), and 3 distinct areas were defined: occupied only in the initial time frame (t = 0) (A), occupied only in the final time frame (t = 10) (C), and overlapping at the initial and final points (B) (Figure 1D and Supplemental Figure 2). A cell deformation index (CDI) was calculated as the ratio (A + C)/(A + B). If the cells were moving vigorously, the area of overlap at the 2 time points (B area) would be small, leading to a higher CDI (Figure 1E), whereas in osteoclasts showing less movement, almost all the area would overlap at the 2 time points, area B would be larger, and the CDI would be lower (Figure 1F).

Because GFP is expressed as a fusion protein with the a3 subunit, GFP fluorescence not only serves as a marker for mature osteoclasts, but it may also provide information on the subcellular distribution of V-type H^+-ATPase in mature osteoclasts if sufficient spatial resolution could be achieved. Because the a3 subunit is an indispensable constituent of the V-type H^+-ATPase pump, connecting transmembrane (V0) and intracellular (V1) portions (14), and is well documented as being involved in H^+ secretion in osteoclasts as well as in other macrophage-lineage cell types (11, 12, 15), it is reasonable to assume that the subcellular distribution of this molecule reflects the functional state of this H^+ pump.

In the 2 polar examples shown in Figure 1, B and C, the different distributions of GFP-V^-type H^+-ATPase are obvious. Static osteoclasts had the ATPase distributed along the sealing zone membranes (Figure 1A), suggesting that they were actively engaged in bone resorption. On the other hand, in osteoclasts undergoing amoeboid movement, the V^-type H^+-ATPases seemed to be distributed diffusely in the cytoplasm (Figure 1A), suggesting these cells would be ineffective at resorption at this moment. Although the distributional changes of GFP-V^-type H^+-ATPases were not necessarily obvious in all osteoclasts imaged due to the limited spatiotemporal resolution of intravital multiphoton bone imaging, it is reasonable from these considerations to consider mobility to be associated with function, i.e., static and moving osteoclasts were resorptive and nonresorptive, respectively. During extended imaging (~40 minutes), some cells changed their CDIs from lower to higher or vice versa (Figure 1G), whereas others remained in a similar CDI state (Figure 1G). These data imply that osteoclasts change their functional activity over time in concert with changes in their motility.

A histogram of CDIs calculated from imaging more than 250 different mature osteoclasts revealed a broad distribution with a wide peak from 0.16 to 0.24 CDI (Figure 1H). Previous reports implied the existence of distinct subsets of mature osteoclasts in terms of their resorptive activity (16). Our imaging data based on tracking a functional reporter (V-type H^+-ATPase) agree with this previous report and characterize these different populations of

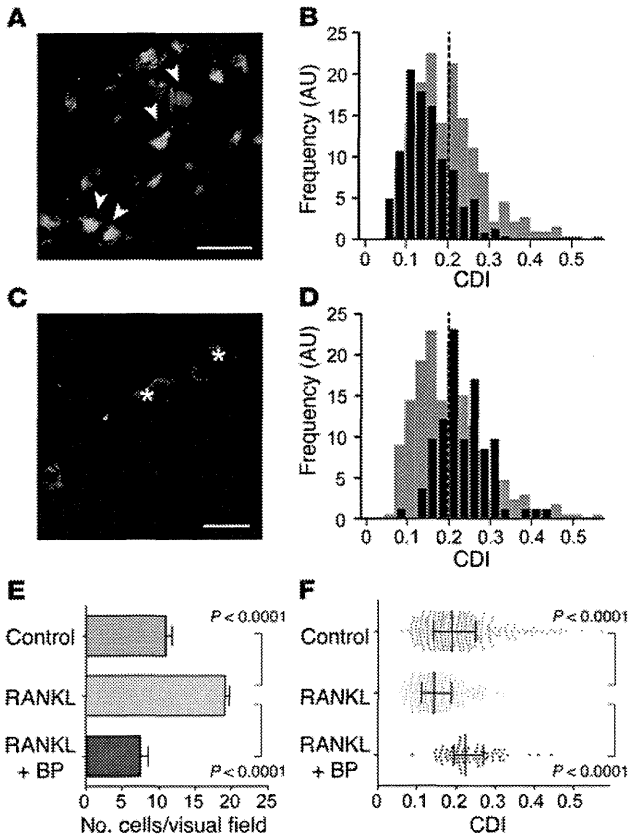

Figure 2
Visualization of mature osteoclasts under pathophysiological conditions. (**A** and **B**) A representative image of live bone imaging of a3-GFP mice after RANKL application (**A**, Supplemental Video 3). Arrowheads indicate a3-GFP at peripheral cell membrane. Scale bar: 40 μm. Histogram of CDIs for osteoclasts imaged under RANKL treatment conditions (black) and control conditions (gray, same as in Figure 1H) (**B**) (n = 224, collected from 5 independent experiments). (**C** and **D**) Representative depiction of live bone imaging of a3-GFP mice after application of RANKL and risedronate (**C**, Supplemental Video 4). Asterisks indicate a3-GFP in cytoplasm. Scale bar: 40 μm. Histogram of the CDIs for osteoclasts imaged under RANKL plus risedronate-treatment conditions (black) and under control conditions (gray, same as in Figure 1H) (**D**) (n = 82, from 5 independent experiments). (**E**) Total number of mature osteoclasts. from 5 independent experiments. (**F**) Distribution of CDI. Data points (n = 259 for control, n = 224 for RANKL, and n = 82 for RANKL plus risedronate) represent individual cells compiled from 5 independent experiments. Error bars represent medians ± interquartile range.

mature osteoclasts as (a) R, (b) N, and (c) intermediate, presumably corresponding to cells actively undergoing a change in state on the bone surface in vivo.

Pretreatment of mice with recombinant RANKL stimulates osteoclastogenesis and reduces bone tissue density (17, 18). In animals treated with this cytokine for 2 days, the total number of mature osteoclasts was increased (Figure 2A and Supplemental Video 3). The CDI histogram showed a left-shifted distribution generally corresponding to the lower end of the motility distribution for cells analyzed under control conditions (Figure 2B), representing an increase in the R population. This interpretation was further supported by the observation that almost all the static osteoclasts showed cell surface expression of GFP-H^+-ATPases in that condition (Figure 2A). On the other hand, application of risedronate, a bisphosphonate (19, 20) used therapeutically to block bone resorption, reduced the total number of mature osteoclasts tightly attached to the bone surface, with many of the remaining cells showing cytoplasmic GFP expression (Figure 2C, and Supplemental Video 4) and with a CDI distribution skewed to the right (Figure 2D), representing an increase in the N population. Statistical analyses demonstrated that treatment with RANKL or RANKL plus bisphosphonate each changed both the total number (Figure 2E) and also significantly altered the CDI distribution (Figure 2F) of mature osteoclasts in vivo. In summary, intravital imaging of mature osteoclasts accompanied with quantitative analyses with CDI enabled us to visualize the functional states as well as the number of mature bone-resorbing osteoclasts in vivo.

To further analyze the different populations of mature osteoclasts, we also generated a chemical fluorescent probe detecting bone resorption at local sites on the bone surface (Supplemental Figure 3A). BAp-E, a boron-dipyrromethene-based (BODIPY-based) H^+-sensing fluorescent probe (pKa ~ 6.2) was conjugated with alendronate, a bisphosphonate, to promote adherence to bone surfaces. The probe coats the bone surface once administered, and green fluorescent signals are detected along the bone surface when mature osteoclasts secrete H^+ for bone resorption and the local pH is decreased. The fluorescence quantum yield (Φ) at pH 7.5 was 0.039, and the Φ at pH 6.0 was 0.29 (the pKa of the fluorescence of the probe was 6.2). Thus, an approximately 7.4-fold increase in fluorescence can be observed for pH changes of this extent (21). We administered this probe to mice in which tdTomato, a red fluorescent protein, is expressed under the promoter of TRAP, a well-known marker for mature osteoclasts (Supplemental Figure 3B). We observed large TRAP-positive (tdTomato) cells on the bone surface, representing mature osteoclasts (Figure 3, A and C, and Supplemental Video 5). Again, we detected 2 different types of labeled osteoclasts in terms of motility, moving (Figure 3A), and static (Figure 3A). Consistent with the data presented above using the GFP–V-type H^+-ATPase–marked cells, green fluorescent signals from the H^+ probes (Figure 3B) overlapped with static but not moving osteoclasts (Figure 3, C and D), supporting the idea that former cells are secreting protons actively and resorbing bone tissues when observed in vivo. We also noticed that there were green dots representing low pH that did not overlap with red osteoclasts (Figure 3C). We think these signals may represent areas previously undergoing active resorption by mature osteoclasts but not covered by osteoclasts at the time of imaging. This interpretation is consistent with in vitro data showing that pitted areas on the bone surface are not always colocalized with osteoclasts (22).

Using these new imaging tools, we next examined the short-term effect of RANKL on the function of mature osteoclasts (Figure 4). Interestingly, less than 10 minutes after i.v. injection of recombinant GST-RANKL, we found that many moving osteoclasts became static cells, suggesting an N-to-R transition without any change in the total number of mature osteoclasts (Figure 4, B and C, and Supplemental Video 6). Because this time course was much faster than that believed required for differentiation or maturation of new osteoclasts in the presence of RANKL, these data indicate that RANKL may have the unexpected property of converting existing mature N into mature R osteoclasts. This concept is compatible with previous literature describing a prompt increase (within 1 hour) in the level of ionized calcium in blood in RANKL-treated mice (23). A lower dose of RANKL